

Modeling of the ECAP Induced Strain Hardening Behavior in FCC Metals



ALI AL-HADI KOBAISSY, GEORGES AYOUB, WAHAZ NASIM, JAHANZAIB MALIK, IBRAHIM KARAMAN, and MU'TASEM SHEHADEH

In this work, a multi-scale framework that couples a crystal plasticity (CP) scheme with a continuum dislocation dynamics (CDD) model is proposed to predict the material behavior, microstructure and texture during equal channel angular pressing (ECAP) processes. The strain hardening in the model is considered to result from both the increase in the dislocation density and the grain fragmentation. The grain fragmentation process is modeled by accounting for the grain-grain interaction and incorporating the concept of the geometrically necessary dislocations (GNDs) into the mean free path of the dislocations. GNDs result from grain boundaries restricting the free deformation of a grain, causing an internal plastic deformation gradient that subsequently leads to grain fragmentation. A commercial Al-1100 billet, with rolling texture, is ECAP processed under Route C for different numbers of passes. Mechanical, microstructure, and texture characterization is achieved for the received and ECAPed materials. The proposed model parameters are calibrated using the tensile true-stress true-strain curves of the unprocessed material at two strain rates. The ECAP-processed aluminum microstructure, texture, dislocation densities and the mechanical properties are predicted.

<https://doi.org/10.1007/s11661-020-05971-2>

© The Minerals, Metals & Materials Society and ASM International 2020

I. INTRODUCTION

ULTRAFINE-GRAINED microstructure in metallic materials is manufactured by using severe plastic deformation methods, which consecutively result in mechanical properties alteration. The most common severe plastic deformation and grain refinement techniques are equal channel angular pressing (ECAP), high-pressure torsion, and accumulated roll bonding.^[1] ECAP is an effective method that was first introduced by Segal in the 1970s^[2] and is used to enhance the mechanical properties by achieving exceptional grain refinement.^[3-5] ECAP is a metal flow process in which a billet is pressed through a die consisting of two channels with equal cross-sections intersecting at an angle Φ . As the billet is pushed through the die, it deforms severely in simple shear mode.^[4] ECAP presents the advantage of processing large samples while maintaining an

unchanged cross-sectional area. Numerous studies on ECAP were conducted to uncover the mechanisms of texture and microstructure alteration induced by grain refinement.^[5-9] ECAP process parameters such as die angle Φ , number of passes, deformation routes, and the back-pressure considerably affect the grain refinement process and hence the texture and the microstructure.^[5,10] The effect of the die angle was studied experimentally at room temperature (RT) on pure aluminum using four different die angles ranging from 90 to 157.5 deg.^[11] For each die angle, the aluminum sample was processed by using several passes while maintaining the final imposed strain at ~ 4 . Ultrafine equiaxed grains microstructure was achieved only with $\Phi = 90$ deg. There are four basic types of routes in ECAP, namely, A, B_a, B_c, and C, as illustrated in Figure 1. Li and Mishin^[12] reported that different deformation routes significantly affect the texture components intensity, which consecutively influence the anisotropic plastic response of aluminum billets. Ferrasse *et al.*^[13] showed that the strength of ECAPed copper samples saturates with the grain refinement slowing down after four passes. In addition, for copper and aluminum billets ECAPed *via* routes A and B, ultrafine subgrain shear bands are observed within the parent grains. Another work by Shaeri *et al.*^[14] reported that after 4 passes *via* routes A and B_c, the ECAPed aluminum presented a very fine microstructure with an average grain size of about 1 and 0.7 μm , respectively.

ALI AL-HADI KOBAISSY and MU'TASEM SHEHADEH are with the Mechanical Engineering Department, American University of Beirut, Beirut, 1107 2020, Lebanon. GEORGES AYOUB is with the Department of Industrial and Manufacturing Systems Engineering, University of Michigan-Dearborn, Dearborn, MI, 48128. Contact e-mail: gayoub@umich.edu WAHAZ NASIM, JAHANZAIB MALIK and IBRAHIM KARAMAN are with the Department of Materials Science and Engineering, Texas A&M University, College Station, TX 77843.

Manuscript submitted March 24, 2020.
Article published online August 25, 2020

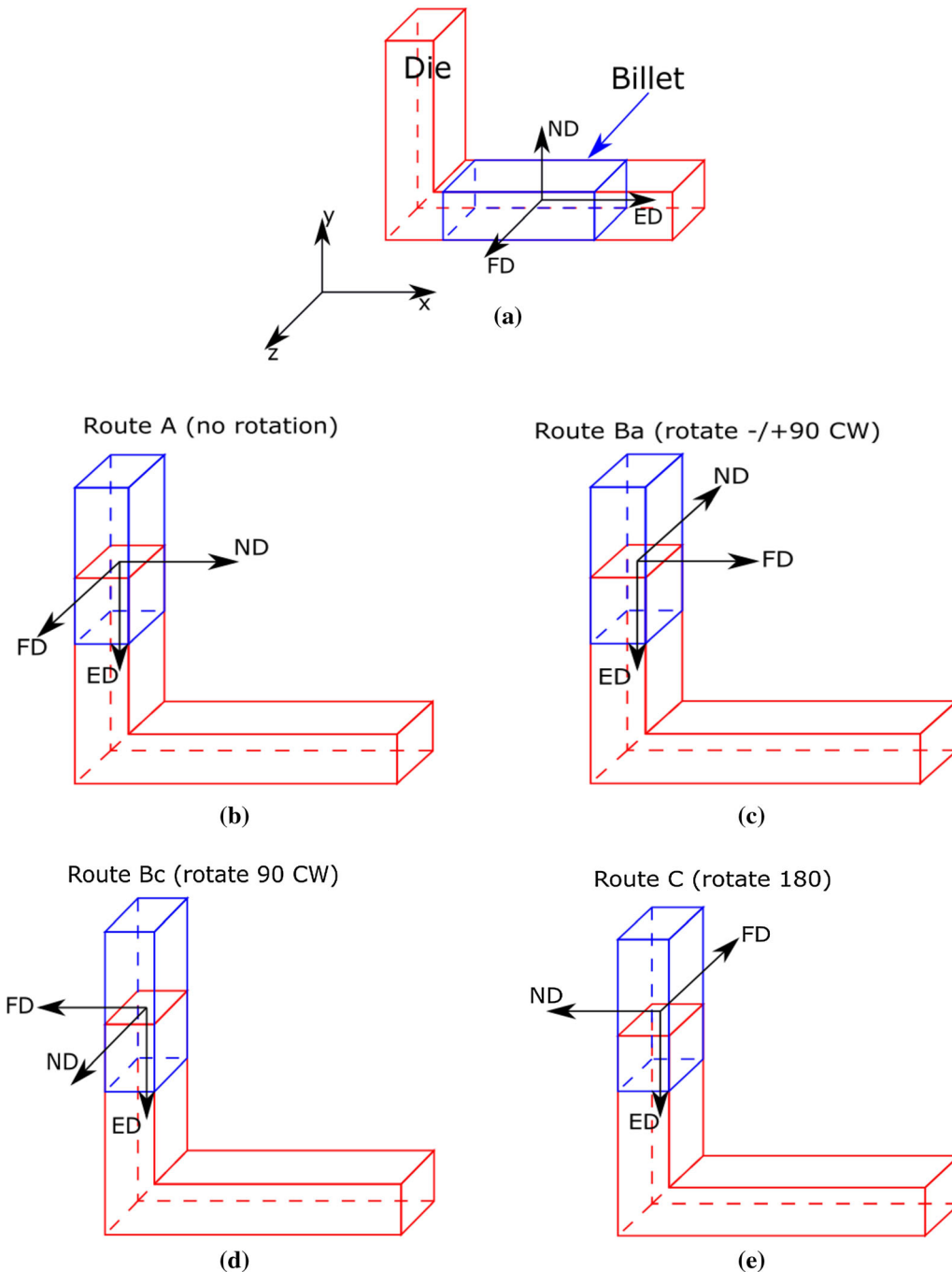


Fig. 1—(a) Simple schematic of the ECAP process, (b) reinsertion of the billet in route A with no rotations between passes, (c) reinsertion of the billet in route B_a with a rotation of 90 deg in alternative directions between consecutive passes, (d) reinsertion of the billet in route B_c with a rotation of 90 deg in the same sense between each pass, (e) reinsertion of the billet in route C with a rotation of 180 deg between passes.

Moreover, the first ECAP pass resulted in strong texture components that weaken after four processing passes. Finally, back-pressure is reported to considerably improve the workability of metallic alloys during ECAP.^[15,16] Stolyarov and Lapovok^[15] reported that the strength and microhardness of aluminum alloy 5083 were significantly improved when ECAP processing with a back-pressure. Krasil'nikov^[16] reported that a pure copper processed by 16 ECAP passes with a back-pressure of 450 MPa resulted in a homogeneous

microstructure with a grain size of $0.19 \mu\text{m}$ and exhibited an ultimate tensile strength of 470 MPa.

Experimental observations on high stacking fault energy materials (SFM), such as Al, showed that the grain refinement is mainly affected by the dislocation slip mechanism.^[17-22] Subgrains are rapidly formed at the initial stage of plastic deformation demarcated by dislocation walls, named geometrically necessary boundaries (GNBs). As plastic strain increases, cell walls formed from the mutual and the statistically

trapped dislocations, divide the parent grain into cell blocks. A misorientation resulting from the difference in the lattice rotation between the cell blocks increases, prompted by the movement of GNB trapped dislocations on different slip systems of the neighboring cell blocks.^[23] In addition, driven by the reorientation of the cell blocks during deformation, some of the low-angle grain boundaries are transformed into high-angle grain boundaries.^[24–27] By continuously increasing the plastic deformation and the misorientation between cell blocks while decreasing the cell block size, lamellar subgrains around interconnecting boundaries are formed.^[20,25,27–29] Furthermore, equiaxed grains start to form leading to finer microstructure.^[22,30,31] Finally, the plastic deformation reaches a steady state when the multiplication and generation of dislocations are balanced by dynamic recovery mechanisms leading to ultrafine equiaxed grain microstructure.^[26,32–36]

Metals are ECAPed at either low or high temperatures, yet, since most cubic metals exhibit good ductility, they are ECAPed at room or warm temperatures. The effect of ECAP temperature was investigated extensively in order to study its influence on microstructural and mechanical development in metals.^[37–41] Chen *et al.*^[37] investigated the effect of different ECAP extrusion temperatures on the evolution of some metallographic parameters of aluminum alloy, such as grain size, grain aspect ratio, and grain boundary misorientation. It was reported that with increasing extrusion temperature, the average grain size gradually increases for temperatures between 50 °C and 250 °C and then a sudden increase is reported for 300 °C, attributed to the significant boundary migration. Additionally, the proportion of low-angle boundaries increases while the proportion of high-angle boundaries decreases with increasing extrusion temperature. The grain shape aspect ratio decreases from 2.7 to 1.5 when the processing temperature is increased from 50 °C to 300 °C, resulting in a more equiaxed grain structure. Chang *et al.*^[40] studied the mechanical properties of 5083 aluminum alloy ECAPed at 200 °C through 8 passes using route C and then tensile tested at room temperature and at 250 °C. At room temperature, the yield strength showed a substantial increase from 129 MPa for the as-received sample to 249 MPa after the first pass and to 290 MPa after 8 passes, while no remarkable variation of the total elongation was observed. However, the Vickers microhardness increased drastically after the first pass, followed by an insignificant variation with an increasing number of passes. The increase of the microhardness after the first pass was attributed to the work hardening associated with the drastic dislocation density increase and the formation of subgrain bands. On the other hand, at high temperature (250 °C), the extruded aluminum alloy showed a decrease in the yield strength from 72 MPa for the as-received sample to 52 MPa after 8 passes, while a considerable increase in elongation (220 pct) was noted after 8 passes. Another study by Prados *et al.*^[41] showed that at room temperature, the yield strength of an ECAPed aluminum alloy through 4 passes increases up to 3 times the yield strength of the unprocessed specimens. Moreover, the ductility is observed to

decrease considerably after the first pass; however, with an increasing number of passes the ductility is recovered and reaches its maximum after the fourth pass. For all tensile samples after ECAP, no work hardening effect was observed. This observation is attributed to two mechanisms, the mutual annihilation and the absorption of the mobile dislocations by the grain boundaries. These mechanisms result in the reduction of mobile dislocation density. They can occur easily in ECAPed materials due to the small diffusion distances^[42] or due to dynamic recovery, which is expected to occur in aluminum at room temperature (30 pct of the homologous temperature).^[43] Although we can find in the literature some experimental characterization of the mechanical properties of ECAPed materials, there is a lack of modeling approaches predicting the mechanical, microstructural, and textural properties of ECAPed materials. Hence, developing physics-based models that predict the properties of ECAPed materials is essential in order to provide insights on the underlying deformation mechanisms.

In the literature, phenomenological- based, dislocation- based or crystal-plasticity-based models were proposed for predicting grain refinement and texture evolution of ECAP-processed materials.^[6,44–55] A phenomenological grain refinement model assuming the self-similarity of the grain refinement process was proposed by Beygelzimer.^[44] The activation of the grain refinement mechanism was initiated with sufficient pressure and strain. A quantitative grain fragmentation process influenced by the strain path complexity was proposed by Petryk and Stupkiewicz.^[48] The proposed model predicted the microstructural changes, grain refinement and strain hardening of FCC metals deformed by ECAP, however the texture evolution was neglected. A volume averaged number of generated dislocations based model was proposed by Starink *et al.*^[47] for predicting the grain refinement during SPD. The formation of new grain boundaries induced by the multiplication of geometrically necessary dislocations (GNDs) and local bond energies dislocations resulting from the effective dislocation-free path and solute–solute nearest-neighbor interactions were predicted.

A disclination-based model describing the grain subdivision mechanism was proposed by Seefeldt *et al.*^[56] Disclinations, by definition, are line defects separating rotated (with slip activity) from unrotated (no slip activity) crystal areas. The microstructure development is described through the disclination model at two different scales, mesoscopic scale (cell block or subgrain level) and microscopic scale (cell or grain level). On the mesoscopic scale, partial disclinations describe nuclei of misorientation resulting from mobile dislocations of the same sign or character being trapped at cell block boundary or cell walls.^[57] On the microscopic scale, parallel dislocation–dislocation interactions lead to the formation of dislocation sheets which in turn lead to the formation of cell walls and thus the formation of new grains.^[56] Nazarov *et al.*^[50,51] implemented the disclination criterion into a visco-plastic self-consistent model to describe the grain subdivision

mechanism. The combination of these two approaches provides information on the formation of disclinations at the grain boundary junctions resulting from the strain incompatibilities between the homogenous effective medium and the grain. Junctions are then transformed into low-angle dislocation boundaries and with further straining they split into new smaller grains.^[51]

Crystal plasticity models were developed also to understand the microstructural and texture development and to evaluate the mechanical response of ECAPed materials.^[46,52,55,58–60] Several aspects were considered in these models, such as the grain size reduction, texture evolution, work hardening, grain shape effect, and grain neighboring effect. Beyerlein *et al.*^[55] proposed a grain fragmentation model based on a visco-plastic self-consistent (VPSC) scheme. Although the proposed model considered the grain shape effect in the fragmentation criteria, it disregarded the influence of the intragranular microstructure. Another physically based approach to model grain fragmentation was proposed by Tóth *et al.*^[46] The proposed model assumed grains to be divided into two zones: the grain center and the grain boundary. The grain boundary, unlike the grain center, was assumed to be slowed down by a friction factor during deformation, leading to lattice curvature development. However, the grain-grain interaction effect was neglected in this model. Inspired by the lattice curvature approach, a recent physically based model was proposed by Kobaissy *et al.*^[58] where the influence of the neighboring grains was taken into account. In this model, the grain-grain interaction effect was described by the accumulation of the geometrically necessary dislocations (GNDs) that were considered as additional material defects accumulated near the grain boundary to accommodate the lattice curvature.^[61–64] In addition, several aspects, including texture evolution, dislocation densities evolutions, and grain fragmentation, were considered. This model was validated on pure copper processed through two ECAP passes and showed a very good agreement with the experimental results. Even though some research efforts were devoted to modeling grain fragmentation, rather less attention was paid to the modeling of the post-mechanical properties of the ECAPed materials. In this work, the post-ECAP mechanical properties of aluminum are predicted by using a modified continuum dislocation dynamics-based model. This paper is organized as follows. The experimental procedure used to ECAP process and characterize the mechanical, microstructural, and texture properties of an aluminum alloy and the experimental results are described in Section II. Section III describes briefly the grain fragmentation model and the grain neighboring effect. In Section IV, the modeling predictions are analyzed and compared with the experiments. Conclusions are provided in Section V.

II. EXPERIMENTAL PROCEDURE AND RESULTS

A commercial Al Al-1100 O-tempered plate with an average grain size of 80 μm and initially low dislocation

density is used. Texture measurements are conducted on the starting material to confirm the typical rolled texture. A composition of 99 at. pct Al purity is utilized to eliminate the occurrence of dynamic precipitation that could occur during ECAP. The plates are machined to 6" long billets with a 1" \times 1" area cross section for the ECAP process.

A. Equal Channel Angular Pressing (ECAP)

All ECAP passes are conducted at room temperature along a 90 deg angled die with a pressing speed of 10 mm/min (strain rate of 10^{-2} s^{-1}) with an applied back-pressure from 2–4 KSI incremented with each pass. Each pass is approximately determined to apply 95 pct strain per pass. ECAP under Route C, with 180 deg clockwise rotation along the extrusion direction after each pass, is conducted for each billet. Single ECAP passes under the 2C and 4C routes are conducted on separate billets to study the evolution of texture, grain size, and mechanical properties.

B. Electron Back Scatter Diffraction (EBSD)

EBSD specimens are cut from the flow plane of the as-received and ECAP-processed billets using electrical discharge machining (EDM). Samples are cut from the middle section of the billet where uniform elongation is normally observed. Samples are mechanically ground on the flow plane surface using SiC paper down to a 1000 grit size. Mechanical polishing is conducted using polycrystalline diamond paste at 3 and 1 μm grit size, followed by a final polish of 0.06 μm colloidal silica. Samples are cleaned using a felt pad and deionized water. EBSD is conducted on a TESCAN FERA-3 SEM under a 15-keV beam voltage. For the rolled condition, a 3 \times 3 mm² area is scanned with a 10 μm step size, while for all ECAP samples a 25 \times 25 μm^2 area is scanned with a 0.1 μm step size. EBSD scans are acquired using Oxford Instruments Aztec software, and post processing, including grain size determination and texture, are conducted on *Oxford Instruments HKL Channel 5 software*. A minimum of 10,000 grains are used to calculate the pole figures and to represent the texture of the as-received and ECAP-processed billets. It is argued that to accurately represent the macrotexture of medium- to moderately textured materials, the orientation data from approximately 10,000 grains generated from EBSD are necessary.

C. Experimental Results

Figure 2 shows the (100), (110), and (111) pole figures of the initial Al-1100 alloy. The (111) pole figure shows a typical cube {001} <100> texture commonly observed in hot-rolled FCC alloys formed due to dynamically recrystallized grains during high-temperature rolling.^[65,66] Some diffuse texture densities are also observed in the (111) pole figure, suggesting that some recrystallized grains may have formed within the shear bands during the rolling process, causing some grains to misorient away from the typical cube texture. Equiaxed

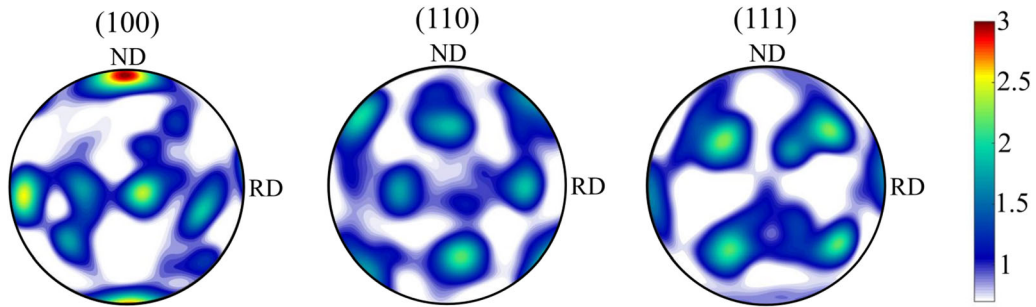


Fig. 2—Pole figures representing the initial texture of Aluminum alloy AA-1100.

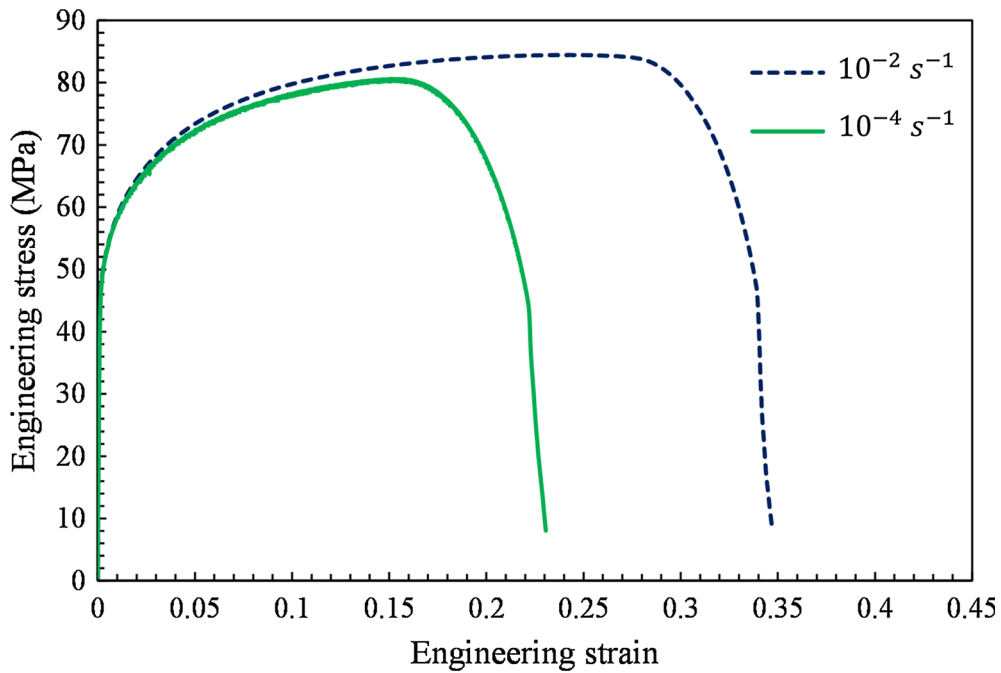


Fig. 3—Measured stress-strain response of the as-received Al-1100 alloy at two strain rates, 10^{-2} s^{-1} and 10^{-4} s^{-1} .

grains within these shear bands could become possible nucleation sites for new recrystallized grains during ECAP with larger misorientations, which could further misorient the grains away from the typical cube texture.^[67]

Figure 3 shows the tensile engineering stress-engineering strain plots at room temperature for the as-received Al-1100 under two different strain rates, 10^{-2} and 10^{-4} s^{-1} , along the rolling direction (RD). The strain hardening response between the two strain rates does not show a significant difference in the experimental tests due to similar slip conditions. Compression tests conducted by other studies on Al1100-O alloys at 10^{-5} to 10^{-1} s^{-1} also showed a similar lack of strain hardening difference within this strain rate window. Strain rate hardening differences were observed only under high strain impact tests with a range of $100\text{--}1000 \text{ s}^{-1}$.^[68] The uniformly elongated region for the 10^{-4} s^{-1} strain rate in Figure 3 occurs at 0.15 strain, compared to the 10^{-2} s^{-1} strain rate at 0.25 strain; hence, strain localization is occurring sooner for the

10^{-4} s^{-1} condition. Due to the symmetric cube texture observed, isotropic strain hardening responses can be assumed for the starting material.

Figure 4 shows the pole figures after tensile deformation at both strain rates. The texture is measured in the uniformly elongated region away from the necked region. Similar texture evolution for the two different strain rates is observed. In both textures, the initially misoriented grains are reoriented closer to the typical cube texture, allowing easy dislocation slip and providing a recovery process for deformed grains. This recovery process is normally observed during rolling deformation of FCC alloys, but this similar mechanism was observed during simple tensile deformation to accommodate higher straining.^[69,70]

Figure 5 shows the ECAP texture of the flow plane for routes 1A, 2C, and 4C. The texture of the 1A ECAP route shows a rigid rotation of 45 deg around the flow direction of the center of the cube texture but maintains the typical cube texture. ECAP was conducted at room temperature; hence, strong grain refinement should be

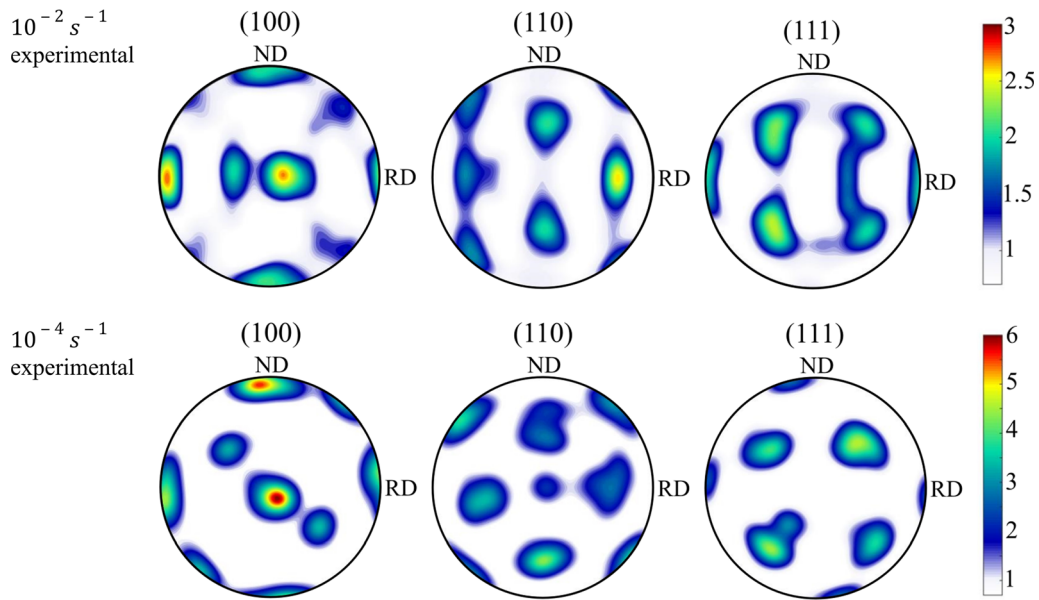


Fig. 4—Measured textures of the tensile as-received samples at two strain rates.

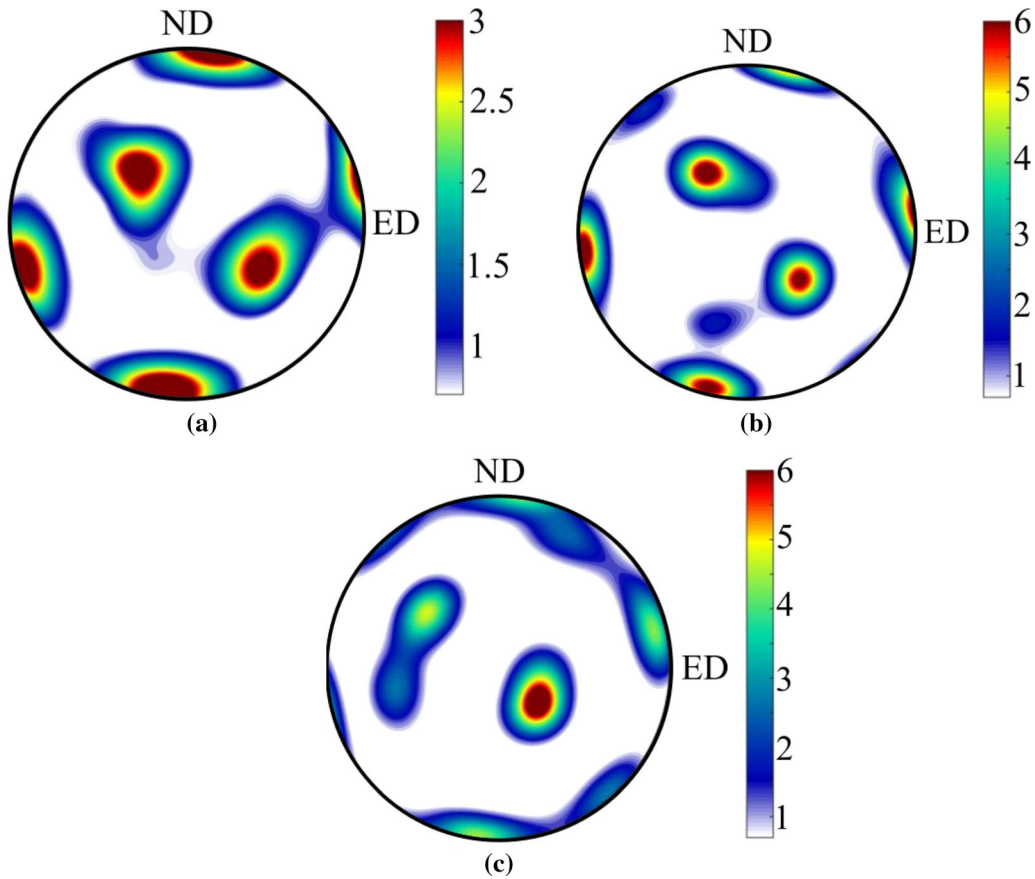


Fig. 5—(111) pole figures of the measured textures after 1 (a), 2 (b), and 4 (c) passes of ECAP *via* route C.

observed with the formation of subgrain and low-angle grain boundaries. The major texture densities show a slight spread in orientation from the main oriented peaks, which show subgrain formation with a

misorientation of 1 to 2 deg and the formation of low-angle grain boundaries with misorientations of 2 to 10 deg. Route C involves rotating the billet by 180 degrees along the extrusion direction between each

ECAP pass. After the first pass, a simple shear along the 45 deg angle produces elongated grains along the shearing direction. On the second pass, due to the 180-degree rotation, an equal and opposite shear strain is applied on the billet, which readjusts the elongated grains to a more equiaxed structure. The comparison between the textures of route 2C and route 1A shows a distinct difference in the low-angle spread of the major texture points in the pole figures. Therefore, subgrain and low-angle grain boundaries are decreased, while high-angle grain (> 10 deg) boundaries are increased. The route 4C texture shows a further increase in high-angle grain boundaries, with the development of new density peaks away from the typical cubic texture. However, the density of low-angle grain boundaries stayed very similar to route 2C. Those grain misorientation distributions are commonly observed in low-temperature ECAP of FCC alloys. Early ECAP deformation (~ 1 to 2 passes) results in subgrain boundary formation with low-angle grain boundaries. Then, with increasing number of passes, more dislocations are deposited along the subgrain, and low-angle boundaries increase the misorientation angle, leading to the development of more low-energy high-angle grain boundaries.^[71]

To investigate the mechanical properties of AA-1100 after ECAP, tensile tests are performed at room temperature. Tensile loading is applied on specimens with their major axes being aligned along either the extrusion direction (ED) or the flow direction (FD) at two strain rates of 10^{-2} and 10^{-4} s⁻¹. A summary of the yield stress (YS), ultimate tensile strength (UTS), and elongation is shown for each ECAP route at 10^{-2} and 10^{-4} s⁻¹ strain rates in Figure 6. The yield and ultimate tensile strengths increased from 50 and 80 MPa to 130 and 150 MPa after one pressing pass and to 160 and 190 MPa after 4 passes, respectively. The higher strength of the ECAPed material is attributed to the

decrease in the grain size (Hall-Petch effect), where the flow stress is inversely proportional to the square root of the grain size. The elongation decreased considerably after one pass and remained almost unchanged with the increasing number of ECAP passes.

Figure 7(a) shows the experimental tensile responses of route 1A at two different strain rates and along two different directions, extrusion and flow. Experimental results show very little strain hardening difference between the two directions and strain rates. This type of hardening behavior was observed for similar Al alloys with ultrafine grain structure. Figures 7(b) and (c) show the experimental tensile responses of routes 2C and 4C, respectively. An increase in the yield stress and ultimate tensile strength is observed with the increase in the number of passes, which can be attributed to the grain refinement and increase in dislocation density. In contrast, a relatively perfect plastic behavior is observed for all ECAP routes (1A, 2C, and 4C). The lack of strain hardening can be due to the high dislocation density reached after ECAP, which allows more dynamic dislocation recovery in FCC alloys during tensile deformation.^[72]

III. MODELING METHODOLOGY

A. Summary of the CP-CDD Approach

During severe plastic deformation, dislocation density increases drastically in the polycrystal, leading to an increase in the internally stored energy. As deformation continues, new grain boundaries are developed, and the internal energy is released by the fragmentation of the parent grain into smaller grains.^[10] In prior work, Kobayashi *et al.*^[58] proposed a grain fragmentation model based on a crystal plasticity (CP) scheme coupled with a continuum dislocation dynamics (CDD) model to capture the microstructural behavior during the ECAP

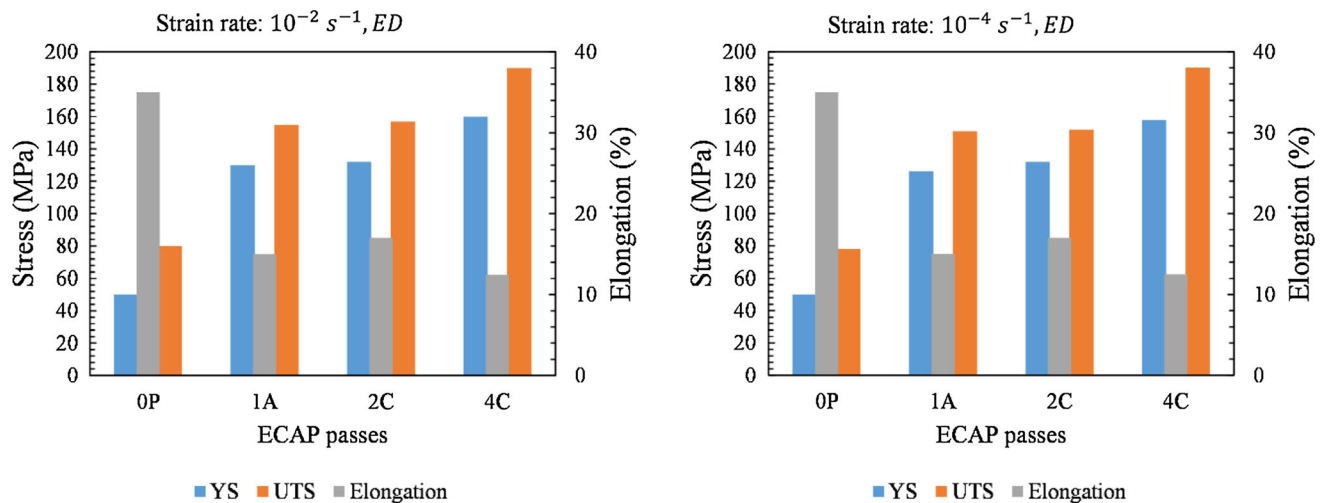


Fig. 6—Experimental tensile behavior data (yield strength (YS), ultimate tensile strength (UTS) and elongation) of the as-received sample (0 pass) and the ECAPed samples after 1, 2, and 4 passes *via* route C at two strain rates. Data values for only the ED tests are shown.

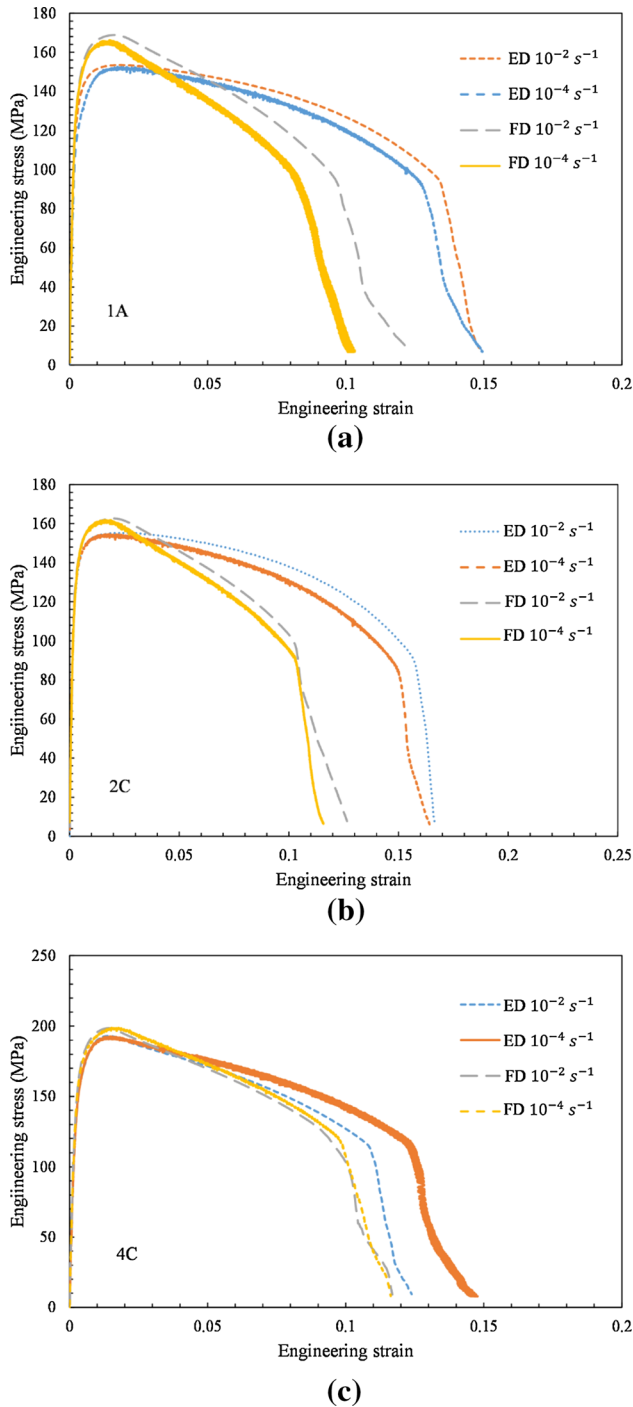


Fig. 7—Engineering stress vs engineering strain plots for the ECAPed Al-1100 alloy at two different strain rates and along two directions for routes (a) 1A, (b) 2C, and (c) 4C. (ED extrusion direction, FD flow direction).

process. The behavior of each crystal is described by crystal plasticity. The Taylor-Lin^[73–75] homogenization scheme is used to capture the overall response of the metallic polycrystal. The polycrystal Cauchy stress is expressed as $T = \frac{1}{N} \sum_{k=1}^N w^k T^k$, where $w^{(k)}$ and $T^{(k)}$ correspond to the weight factor and the Cauchy stress of the

k th crystal, respectively, and N is the total number of crystals. In this scheme, the addition of the elastic $l_e^{(k)}$ and the plastic $l_p^{(k)}$ velocity gradient tensors in each grain is assumed to be equal to the macroscopic velocity gradient $L (l_e^{(k)} + l_p^{(k)} = L)$. The stress in a metallic single crystal is defined by the second Piola–Kirchoff stress tensor, which is expressed as $T^* = \mathcal{L} \cdot E^e$, where \mathcal{L} is the fourth-order stiffness tensor of the single crystal and E^e is the elastic Green–Lagrange strain tensor. The Cauchy stress in each crystal can be written then as $T^{(k)} = \frac{1}{\det F^e} F^e T^* F^{e-T}$. In this work, F represents the deformation gradient tensor, which can be decomposed multiplicatively into elastic F^e and plastic F^p deformation gradient tensors as $F = F^e F^p$.^[76] The evolution of the plastic deformation gradient F^p can be expressed in terms of the plastic velocity gradient tensor L^p as follows: $\dot{F}^p = L^p F^p$, with $L^p = \sum_{s=1}^{12} \dot{\gamma}^s S^s$ for materials deforming only by slip. $\dot{\gamma}^s$ is the slip shear rate on the slip system “s” and $S^s = m_0^s \otimes n_0^s$ is the Schmid tensor, where m_0^s and n_0^s are the slip direction and the slip plane normal of the “s” slip system, respectively.

A continuum dislocation dynamic model is coupled with the crystal plasticity model for the purpose of capturing the evolution of dislocation densities. The Orowan relationship^[77] is used to describe the effect of mobile dislocation density and glide velocity in the formulation of the plastic shear rate: $\dot{\gamma}^s = \rho_m^s b v_g^s$, where ρ_m^s is the mobile dislocation density in the slip system “s” and b is the magnitude of the Burger vector. The dislocation glide velocity v_g^s on system “s” can be written

as $v_g^s = v_0 \left| \frac{\tau^s}{\tau_{th}^s} \right|^{1/\eta} \text{sign}(\tau^s)$, where v_0 is the reference velocity, η is the strain rate sensitivity factor, τ^s is the resolved shear stress on slip system “s”, and τ_{th}^s is the threshold resolved stress of the slip system “s”. τ_{th}^s can be decomposed additively into three stresses, the initial critical resolved shear stress τ_0 , the Hall-Petch stress τ_{HP}^s , and the shear stress responsible for the material hardening τ_H^s . Hence, the threshold stress on each slip system “s” is expressed as $\tau_{th}^s = \tau_0 + \tau_{HP}^s + \tau_H^s$. The Hall-Petch stress is expressed in terms of the Hall-Petch parameter K and grain size D as $\tau_{HP}^s = K^s D^{-0.5}$. In addition, the hardening stress resulting from the long-range interactions between dislocations is expressed as

$\tau_H^s = \sum_{r=1}^{N_{si}} \Omega^{sr} \alpha_{BH} G b \sqrt{\rho_{TSS}^r}$, where Ω^{sr} is the interaction matrix, α_{BH} is the Bailey-Hirsch coefficient, G is the shear modulus, N_{si} is the number of slip systems that interact with the slip system “s”, and ρ_{TSS}^r is the total statistically stored dislocation density, defined as the sum of the mobile (ρ_m^r) and the immobile (ρ_i^r) dislocation densities in the slip system “r” ($\rho_{TSS}^r = (\rho_m^r + \rho_i^r)$). During plastic deformation, both the mobile and the immobile dislocation densities can evolve. The evolution laws for these two quantities are described by Li *et al.*^[78] and are represented below in Eqs. [1] and [2].

$$\begin{aligned} \dot{\rho}_m^s &= \alpha_1 \rho_m^s v_g^s / \bar{l} - 2\alpha_2 R_c (\rho_m^s)^2 v_g^s - \alpha_3 \rho_m^s v_g^s / \bar{l} \\ &+ \alpha_4 (|\tau^s| / \tau_{th}^s)^\zeta \rho_i^s v_g^s / \bar{l} + \alpha_5 \sum_{\beta=1}^{N_{cs}} P^{s\beta} \rho_m^\beta v_g^s / \bar{l} \\ &- \alpha_6 R_c \rho_m^s \rho_i^s v_g^s \end{aligned} \quad [1]$$

$$\dot{\rho}_i^s = \alpha_3 \rho_m^s v_g^s / \bar{l} - \alpha_4 (|\tau^s| / \tau_{th}^s)^\zeta \rho_i^s v_g^s / \bar{l} - \alpha_6 R_c \rho_m^s \rho_i^s v_g^s \quad [2]$$

In these equations, \bar{l} is the mean free path of dislocations, R_c is the critical radius for dislocation annihilation, $P^{s\beta}$ is the matrix that describes the probability for the cross-slip mechanism to occur, and ζ is a constant set as 0.5. Six dislocation mechanisms contributing to the hardening behavior of the material are described by the rate Eq. [1], which depends on six material parameters ($\alpha_1 - \alpha_6$). The first term captures the rate of multiplication and generation of mobile dislocations resulting from the propagation of resident dislocations and the production of new dislocations due to Frank-Read sources. The second term describes the annihilation of two mobile dislocations of opposite signs. The immobilization of mobile dislocations due to the formation of dipoles and junctions is captured in the third term, while the mobilization of immobile dislocations due to the breakup of pinning points, junctions, and dipoles is described in the fourth term in Eq. [1]. The fifth term accounts for the cross-slip mechanism that occurs when a screw dislocation on one slip plane jumps to another slip plane during plastic deformation. Finally, the annihilation of mobile and immobile dislocations due to their interaction is presented in the sixth term.

B. Grain Fragmentation Modeling

Severe plastic deformation alters the microstructural and texture properties of polycrystalline materials by evolving the dislocation density and grain size. In the proposed approach, material hardening results from the evolution of the dislocation density and reduction of the average grain size that hinder the movement of dislocations. We differentiate between two types of dislocations: the statistically stored dislocations (SSDs) and the geometrically necessary dislocations (GNDs). SSDs are dislocations that are randomly trapped within a grain, while GNDs are dislocations that accumulate near the grain boundaries. GNDs account for the effect of the neighboring grains by the additional storage of materials defects that hinder the movement of mobile dislocations and thus reduce their mean free path. SSDs give rise to homogeneous stress and strain fields,^[79] while GNDs contribute to an inhomogeneous state of stress and strain that accommodates the lattice curvature during the non-uniform plastic deformation.^[80] The GND effect is implemented in the mean free path of the moving dislocations and written as follows^[81,82]:

$$\bar{l} = \frac{c^*}{\sqrt{\sum_{j=1}^{N_{si}} w^{js} (\rho_{TSS}^j + \rho_{GND}^j)}} \quad [3]$$

where c^* is scale factor accounting for the non-uniformity of the dislocations distribution in the crystal, w^{js} is a weight matrix fully populated by ones for simplicity, and ρ_{GND}^j denotes the density norm of GNDs on slip system “ j ” and is expressed in terms of the Nye’s tensor α_{nm}^j corresponding to slip system “ j ”^[83,84] as,

$$\rho_{GND}^j = \frac{1}{b} \sqrt{\alpha_{nm}^j \alpha_{nm}^j} \quad [4]$$

The evolution of the Nye’s tensor for large deformation is described as the gradient of the plastic velocity gradient using the L^P :

$$\dot{\alpha} = \text{curl}(L^P) \text{ or } \dot{\alpha}_{ij} = e_{jkl} L_{il,k}^P \quad [5]$$

where e_{jkl} denotes the permutation tensor. $L_{il,k}^P$ is the derivative of the plastic velocity gradient and is obtained using the central difference method.^[79]

A grain fragmentation model was recently proposed by Kobaissy *et al.*^[58] to predict the microstructural, texture, and mechanical behavior of cubic material during ECAP. The model was based on the lattice curvature approach proposed by Tóth *et al.*^[46] and extended to account for the grain-grain interaction. Furthermore, with increasing plastic deformation, the Kobaissy *et al.*^[58] approach accounted for the development of the misorientation angle between the center of a grain and its boundary. When a threshold misorientation angle was reached (*i.e.*, 5 deg), the subgrains were then considered as new grains with different orientations from their parent grain. The model assumed that a grain fragments into four grains of equal size. In this work, the grain fragmentation procedure is improved to better mimic the experimental observations: a grain is subdivided into nine subgrains with a grain-boundary-free central subgrain. The subgrains are assigned their parent grain orientation before deformation. The subgrains are considered as new grains when the fragmentation criterion is satisfied (misorientation angle exceeds 5 deg). Each parent grain is allowed to split up to a maximum of $9 \times 9 \times 9 = 729$ new grains (3 fragmentation levels) (Figure 8(a)). Depending on the neighboring grains, the subgrains of a parent grain can exhibit different levels of fragmentation. In our simulations, the initial polycrystal microstructure is discretized into a uniform 2D grid of squared grains, as represented in Figure 8(b). Each grain in the grid is assigned a grain size, orientation, initial dislocation density, and position whereby the neighboring grains are identified. It is assumed that the middle subgrains are not affected by the neighboring grains, while the neighboring grains’ effect is accounted for in the deformation calculation of the remaining subgrains by adding the GND effect. It is also assumed that the accumulation of GNDs at the grain boundary is associated with the induced misorientation angle according to the relation proposed by Konijnenberg *et al.*

$$\theta_m = \rho_{GND} * D * b / 3 \quad [6]$$

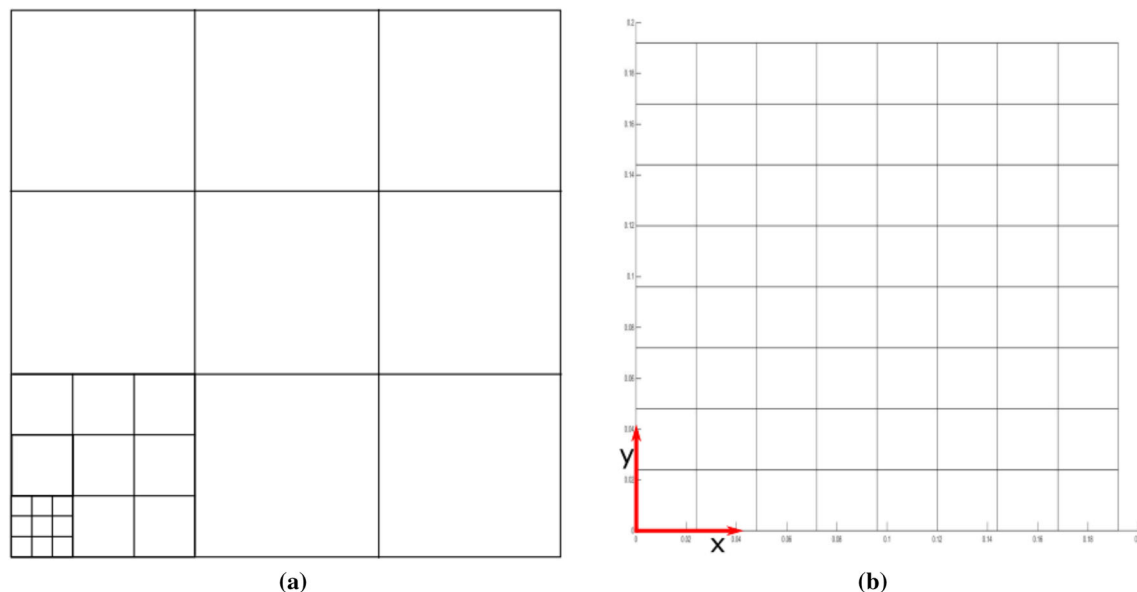


Fig. 8—(a) Subdivision of grain into $9 \times 9 \times 9$ subgrains, and (b) schematic representation of the polycrystal.

where D is the grain size and b is the magnitude of the Burgers vector.

IV. RESULTS AND DISCUSSIONS

In this section, the numerical results are presented, analyzed, and compared with the experimental ones. First, the model parameters are identified by fitting both the tensile stress-strain response and the texture results. The identified model parameters are then used to conduct ECAP simulations with route C through a different number of passes. The predicted texture evolution is then compared to the experimental results, and the strain hardening, dislocation density evolution, and slip system activity are extracted. Finally, the mechanical behavior of the ECAPed aluminum is simulated and compared to the experimental mechanical behavior results.

A. Calibration of Model Parameters

The initial microstructure of the polycrystal aluminum alloy presented an average grain size of $80 \mu\text{m}$, and its initial texture, represented by the (100), (110), and (111) pole figures, is shown in Figure 2. The model parameters are identified by fitting the simulated tensile true stress-true strain curves and the resulting texture to the experimental ones. As mentioned previously, the tensile tests were conducted at room temperature along the rolling direction for two different strain rates, 10^{-2} and 10^{-4} s^{-1} . The deformation gradient tensor can be written as:

$$F = \begin{pmatrix} e^{\dot{\epsilon}\tau} & 0 & 0 \\ 0 & e^{-\dot{\epsilon}\tau/2} & 0 \\ 0 & 0 & e^{-\dot{\epsilon}\tau/2} \end{pmatrix} \quad [7]$$

where $\dot{\epsilon}$ is the strain rate and τ is the time increment.

The comparison between the experimental and the numerical tensile true stress-true strain curves is presented in Figure 9. An excellent agreement between the numerical and the experimental results for both strain rates is observed. It is worth mentioning that the model parameters are calibrated on the experimental results interrupted at the ultimate tensile strength (UTS), since the stress state deviates from the uniaxial loading condition with the propagation of the plastic instability. The UTS values for the 10^{-2} and 10^{-4} s^{-1} strain rates are equal to 93 and 107 MPa, respectively.

The numerical texture is also compared to the experimental textures for both tensile loading conditions (the texture is measured in the gage length away from the necking area). Figure 10 shows the capability of the model to reproduce all the main texture components. The difference in the intensity levels may be attributed to the difference in the number of grains used to plot the pole figures. Table I lists the model parameters that are used to generate the optimal fit between the numerical and the experimental results. The initial SSD and GND densities values are taken as 2.4×10^{13} and $1.2 \times 10^{14} \text{ m}^{-2}$, respectively.

B. Prediction of ECAP

1. Texture

The polycrystal texture changes significantly with the severe plastic deformation induced by the ECAP process. The considerable change in the texture results in an evolution of the material's mechanical and anisotropic properties. Several processing factors, such as processing route, number of passes, die angle, *etc.*, affect the evolution of the texture. In this work, aluminum alloy is ECAPed up to four passes through route C. A Taylor-Lin model combining crystal plasticity and

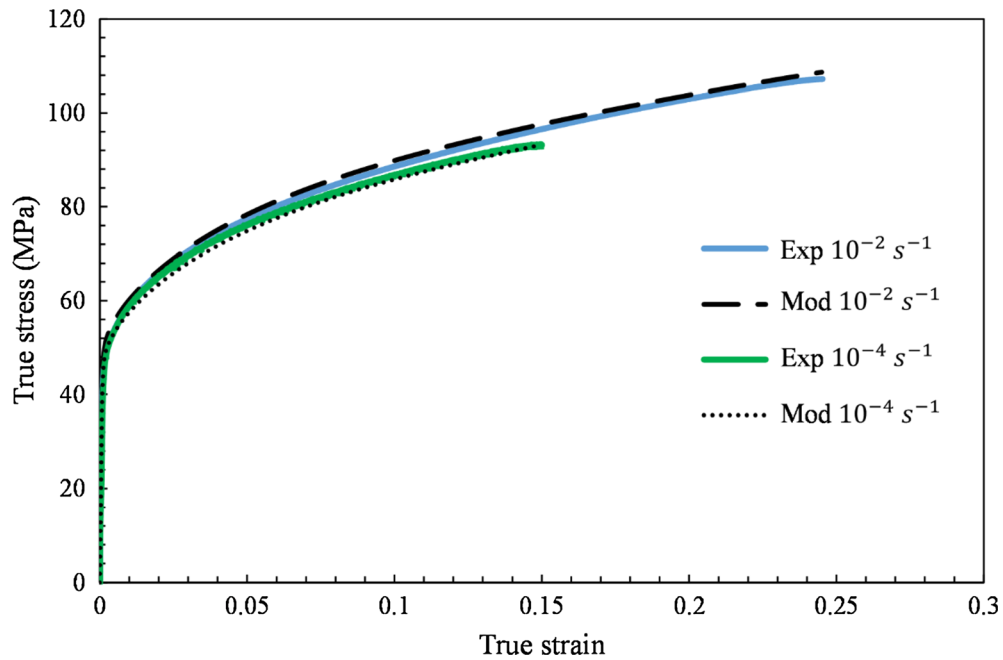


Fig. 9—Experimental and simulated true stress-true strain behaviors at two different strain rates 10^{-2} and 10^{-4} s^{-1} .

continuum dislocation dynamics approaches is used to predict the texture evolution during ECAP. The predicted and the experimental texture are compared by analyzing the presence and location of the ideal orientations of the shear texture listed in Table II.

The ideal orientations of ECAP textures were studied by several investigations^[85,86] and found to be CCW-rotated by an angle $\theta = \Phi/2$ around the flow direction (FD) in the (111) pole figure. The main ECAP texture components, similar to simple shear texture components, are distributed along fibers in the orientation space and are represented in the (111) pole figure in Figure 11.^[87] Figure 12 shows the experimental and the predicted textures after one pass of ECAP. The experimental texture is measured using the electron back-scattered diffraction (EBSD) method and then plotted, similarly to the predicted texture, using the MTEX software. A good agreement between the experimental and the predicted texture can be noticed; furthermore, the predicted texture exhibits all the ideal ECAP texture orientation components. All ideal components are captured by the model; however, A_θ/\bar{A}_θ components are missing from the measured texture. In addition, some intensity-level differences between the two textures are observed, which may be attributed to the different number of grains used to plot the pole figures.

The post-mechanical properties of aluminum ECAPed through route C after four passes are studied. Under route C, also called the reversal route, the shear direction is reversed between consecutive passes while maintaining the same plane of shearing. The texture symmetry under route C is maintained as long as the sample's deformation is kept homogeneous and the sample is rotated around the axis of symmetry (FD). This texture symmetry, also called monoclinic symmetry, exhibits a shear-like texture in which the texture

after even-numbered passes is recovered and the textures after odd-numbered passes resemble the first-pass texture.^[10,88] The measured and predicted textures of the aluminum ECAPed through route C after two and four passes are presented in Figure 12. The ideal shear texture components are observed in the measured textures of the 2C and 4C ECAPed aluminum. Furthermore, a good agreement with the predicted texture is observed, with a difference in the intensity levels of a factor of two.

2. Strain-hardening behavior

In the last decade, modeling the strain-hardening behavior of materials subjected to severe plastic deformation was of interest in many investigations. Dislocation-based models were proposed for that purpose.^[46,89-91] Using the continuum dislocation dynamics-based grain fragmentation model,^[58] the *in-situ* mechanical response of the material during the ECAP process is predicted. Figure 13 depicts the predicted von Mises stress-von Mises strain curve as well as the strain hardening rate vs von Mises strain for the four ECAP passes. The predicted strain-hardening behavior follows the expected behavior of a polycrystalline material as reported in the literature.^[46,91] Although the elastic region (ends at a strain of 0.2 pct) is very small compared to the plastic region, the elastic behavior is predicted by our simulations, since the elastic deformation is accounted for by the Taylor-Lin CP-CDD model. Initially, the strain-hardening rate shows a fast linear decrease up to 20 pct of strain, followed by a slower continuous decrease until the end of the first pass. The decrease in the strain-hardening rate with increasing strain was suggested to be induced by the dynamic recovery process.^[91] Figure 13 shows that the 1A aluminum exhibits a different

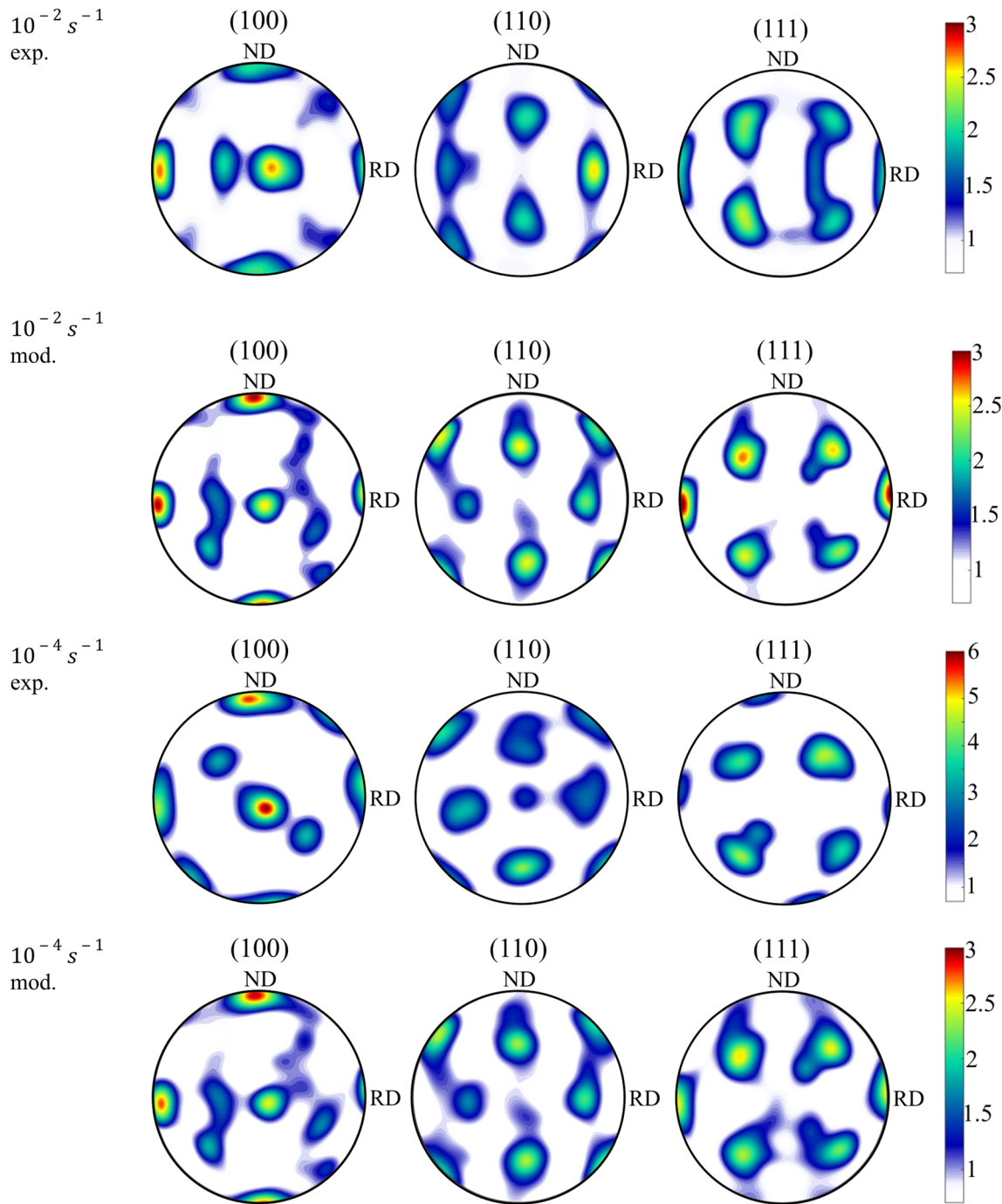


Fig. 10—Comparison of the measured and the simulated textures of the tensiled as-received samples at two strain rates. Note the experimental results are repeated here for the sake of visual comparison.

strain-hardening behavior when ECAPed through route C, compared to the as-received material when ECAPed. The different hardening behavior is attributed to the evolution of the microstructure and texture after the 1A ECAP pass, where the majority of the grains are rotated to their ideal positions, which leads to a decrease in the Taylor factor.^[92] In the 2C pass, the rate of strain hardening decreases rapidly until it reaches a plateau-like behavior after a strain of 20 pct. In the third ECAP pass, Figure 13 shows a decrease in the yield stress and a

linear strain-hardening behavior due to the texture developed in the second pass, where the billet is rotated by 180 deg between consecutive passes. The strain-hardening behavior in the fourth pass mimics the behavior in the second pass, which can be explained by the monoclinic symmetry after even passes *via* route C, as illustrated in Section IV-B-1.

During plastic flow, the dislocation motion is affected either by short-range barriers, such as vacancies and interstitial atoms, or by long-range barriers, such as

Table I. List of Properties and Calibrated Model Parameters of Aluminum Alloy

Parameter	Definition	Value (Unit)
C_{11}, C_{12}, C_{44}	elasticity constants	1,06,800, 60,700, 28,000 MPa
μ	shear modulus	26,000 MPa
K	Hall–Petch coefficient	1.0 MPa mm ^{1/2}
D	average grain size	80 μ m
b	magnitude of burgers vector	2.86×10^{-10} m
$\dot{\epsilon}$	strain rate	0.01 s ⁻¹ for ECAP
τ_0	initial critical resolved shear stress	12 MPa
η	strain rate sensitivity	0.01
c^*	numerical constant	0.8
q	ratio of the latent hardening rate to the self-hardening rate	1.4
v_0	reference strain rate	0.001 m/s
α_{BH}	Bailey–Hirsch hardening coefficient	0.07
α_1	dislocation multiplication coefficient	0.02
α_2	dislocation annihilation coefficient	1.0
α_3	immobilization coefficient	0.002
α_4	mobilization coefficient	0.002
α_5	cross-slip coefficient	0.003
α_6	mobile-immobile annihilation coefficient	1.0
$\rho_{m-i}^{initial}$	initial mobile dislocation density on slip system i	10^{12} m ⁻²
$\rho_{i-i}^{initial}$	initial immobile dislocation density on slip system i	10^{12} m ⁻²
$\rho_{GND}^{initial}$	initial geometrically necessary dislocation density	10^{13} m ⁻²

Table II. Main Ideal Orientations, Represented by Their Euler Angles and Miller Indices, of FCC Crystals in ECAP with Die Angle $\Phi = 90$ deg

Notation	Euler Angles (Deg)			Miller Indices		
	φ_1	ϑ	φ_2	ED	ND	FD
$A_{1\theta}^*$	80.26	45	0	[441]	[118]	[110]
$A_{2\theta}^*$	170.26	90	45	[118]	[441]	[110]
A_{θ}	9.74	45	0	[118]	[441]	[110]
\bar{A}_{θ}	99.74	90	45	[914]	[1115]	[112]
B_{θ}	45	35.26	45	[914]	[1115]	[112]
\bar{B}_{θ}	225	35.26	45	[15 4 11]	[7 26 19]	[111]
C_{θ}	45	54.74	45	[15 4 11]	[7 26 19]	[111]
\bar{C}_{θ}	165	54.74	45	[334]	[223]	[110]
$A_{1\theta}$	225	54.74	45	[334]	[223]	[110]
$A_{2\theta}$	135	45	0	[334]	[223]	[110]
$\bar{A}_{2\theta}$	45	90	45	[334]	[223]	[110]

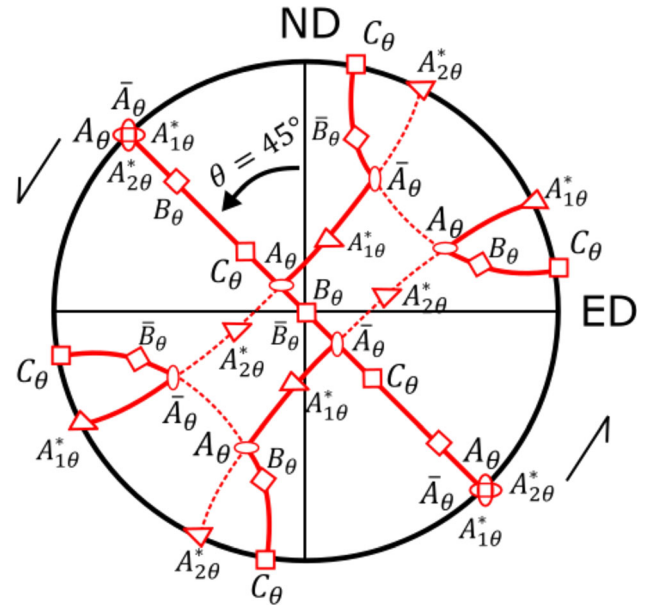


Fig. 11—(111) key pole figure representing the ideal orientations after one pass of ECAP.

grain/subgrain boundaries and forest dislocations. Low-angle boundaries subgrains are formed by the accumulation of dislocations. The immobilization of dislocations at the subgrain boundaries results in an increase of the misorientation angle and hence the formation of new grains. The dislocation density evolution is influenced by the microstructural change (grain size decrease) induced by the severe plastic deformation. In fact, the movement of the mobile dislocations is hindered by the increasing volume of grain boundaries.^[93] Recently, several studies^[94–98] characterized the microstructural evolution of aluminum alloys and measured the dislocation density for several ECAP passes *via* different routes. The studies reported a major

increase in dislocation density after the first pass where grain fragmentation is the main deformation mechanism. However, a gradual increase was reported for the subsequent passes. Based on the literature,^[94–98] the SSD density was reported to reach a value of 2.4×10^{14} m⁻² after the first pass, which is less than the value predicted by our proposed model. We can explain the difference between the experimental and predicted SSD density by the fact that the proposed model does not account for the dynamic recovery process contributing to moderate the plastic hardening during ECAP

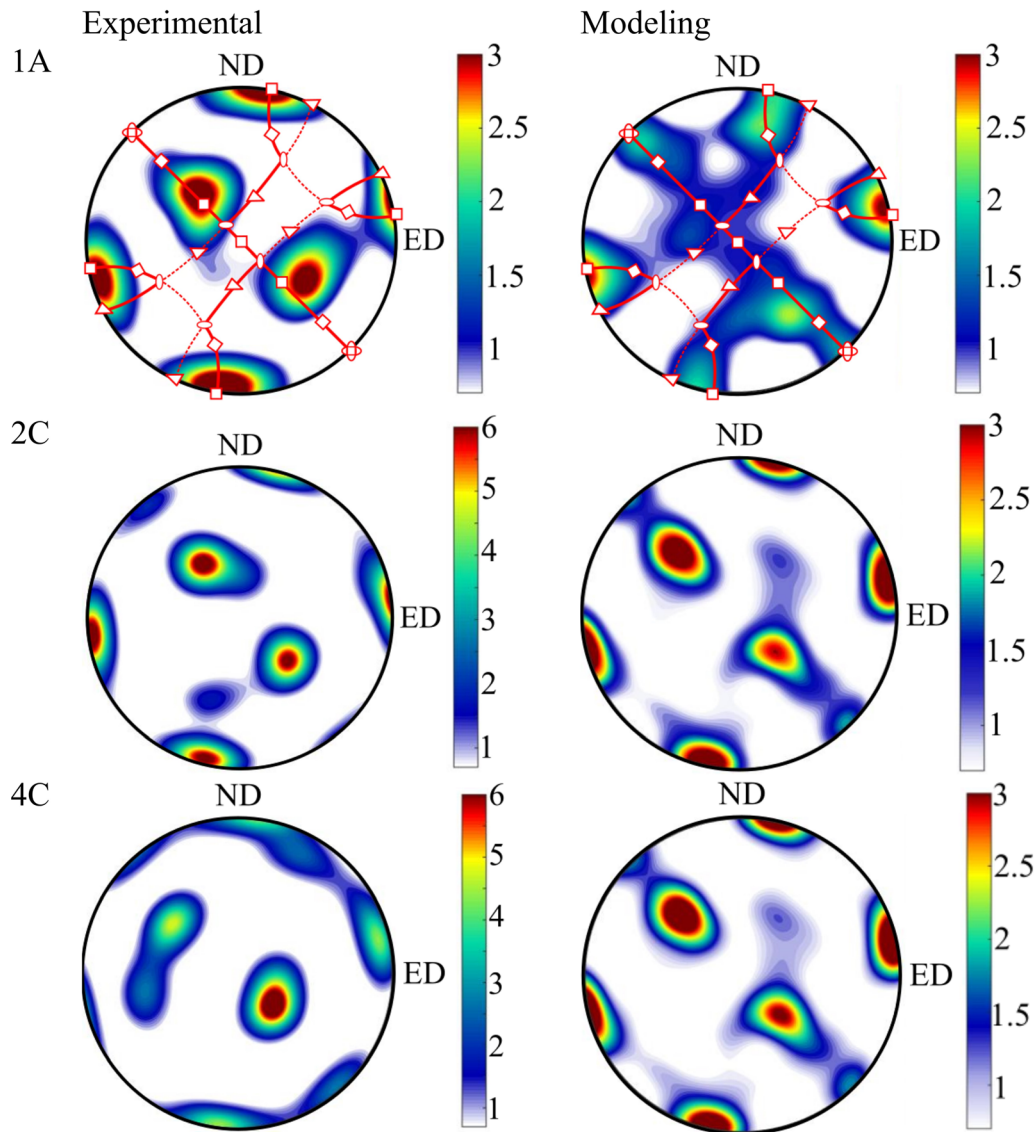


Fig. 12—(111) pole figures of the measured and predicted textures after 1, 2, and 4 passes of ECAP *via* route C. Note the experimental results are repeated here for the sake of visual comparison.

processing. A recovery factor is applied before each pass to reduce the dislocation density and hence account indirectly for the dynamic recovery process. The same recovery factor of the dislocation density between passes under route C (same as Reference 94) is assumed; thus, the dislocation density values are 3×10^{14} and $3.6 \times 10^{14} \text{ m}^{-2}$ after the second and the fourth pass of ECAP *via* route C.

Figure 14 shows the evolutions of mobile, immobile, and geometrically necessary dislocation densities as a function of the strain for the different ECAP passes. During the 1A pass, the densities of the mobile dislocations and the GNDs exhibit a similar evolution, although the initial value of the GND density is 10 times greater than that of the mobile dislocation density. During the 1A pass, grains are subjected to severe plastic deformation, which drastically increases their internal energy, leading to grain fragmentation as a

relief mechanism. Consequently, the coarse grains are fragmented into smaller grains exhibiting different dislocation densities than the parent grains. The increase in the dislocation density is predicted in Figure 14, where both mobile dislocations and GNDs increase similarly up to a strain of 80 pct. After this strain value, most of the grains are fragmented, so the mobile dislocation evolution rate decreases since the GNDs now act as obstacles at the grain boundaries. During each pass, the generation and the multiplication of dislocations will lead to an increase in the dislocation density, which is predicted by the current model in Figure 14.

3. Slip Activity

Dislocation motion usually occurs on a specific slip system, which is a combination of slip plane and slip direction. The movement of dislocations initiates the

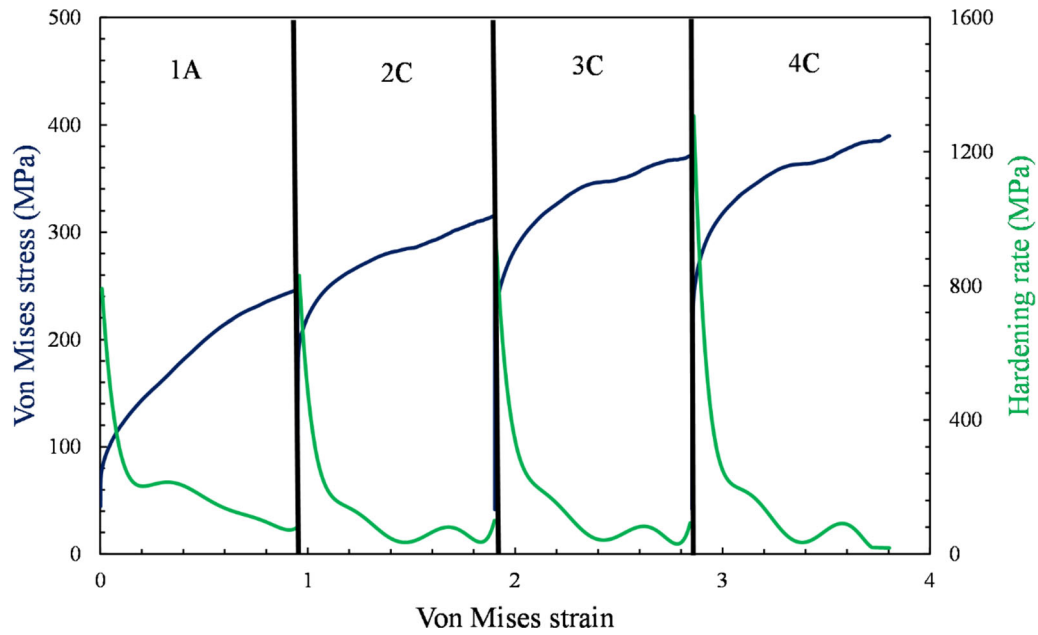


Fig. 13—Predicted hardening behavior of aluminum alloy during four passes of ECAP.

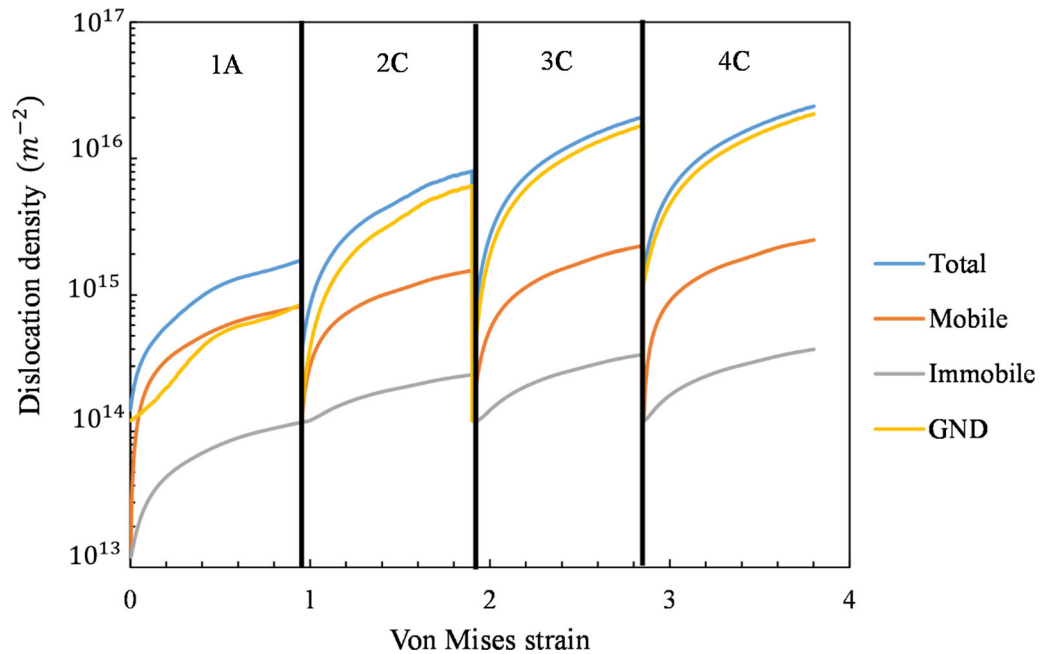


Fig. 14—Dislocation density evolution during the four passes of ECAP.

plastic deformation, implying that several slip systems are activated. In FCC metals, twelve slip systems $\{111\}\langle 110 \rangle$ may be activated when the resolved shear stress on a specific system exceeds the critical resolved shear stress, which is responsible for a dislocation movement. In the present work, crystallographic slip is assumed to be the main deformation mechanism that induces plasticity. The activity of slip systems affects the texture evolution and the lattice reorientation.^[99] Figure 15 shows the relative activity of the 12 slip systems, represented by the four slip planes, obtained

numerically for the four passes of ECAP. The relative activity on slip system “s,” RA^s , is calculated as the average of the slip system activity for all grains in the polycrystal^[100]:

$$RA^s = \frac{\sum_{N=1,Ng} \dot{\gamma}^s(N) * w(N)}{\sum_{j=1,12} \sum_{N=1,Ng} \dot{\gamma}^j(N) * w(N)} \quad [8]$$

where Ng is the total number of grains and w is the weight factor of the grain.

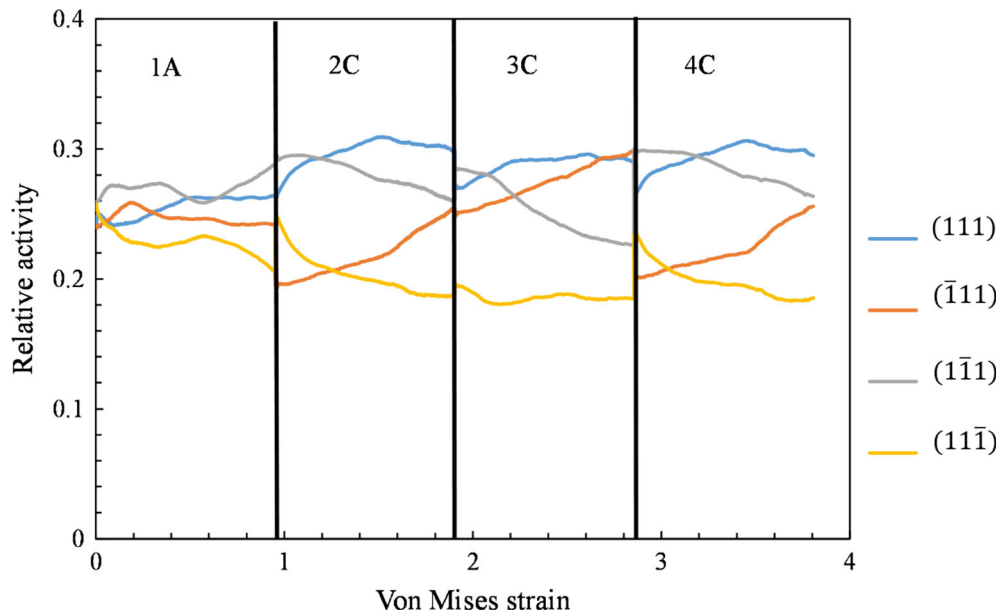


Fig. 15—Relative slip system activities during ECAP.

For all passes, all of the slip systems are activated, with some slip systems dominating others. In the first pass, all slip planes have approximately similar relative activities up to 50 pct, after which the $(\bar{1}\bar{1}1)$ slip plane becomes more active and the $(1\bar{1}\bar{1})$ slip plane becomes less active, while (111) and $(\bar{1}1\bar{1})$ remain unchanged. Other slip systems show an almost stable relative activity during the first pass. Different relative activities are shown in the second pass due to the developed texture and to the rotation of the billet by 180 between ECAP passes. We can notice that the relative activities of the $(\bar{1}\bar{1}1)$ and $(\bar{1}1\bar{1})$ slip planes exhibit an opposite evolution. The relative activity of the $(\bar{1}1\bar{1})$ slip plane shows a noticeable increase with strain, while the relative activity of $(1\bar{1}\bar{1})$ slip plane shows a slight decrease with strain. The slip planes' activity variations could be explained by the multiplication and annihilation of dislocations on those slip systems. Figure 15 shows a similar relative activity evolution for the different slip planes in the 2C and 4C passes, since a similar initial texture is used for both passes due to the texture symmetry in route C after an even number of passes. In contrast, different relative activity evolutions are observed for the 3C pass since the initial texture of the billet is rotated 180 deg.

During ECAP, the shearing plane, defined at the two intersecting ECAP channels, are the macroscopically most stressed plane. Thus, dislocations with different Burgers vectors are developed mainly at this plane and its surrounding in which slip systems are active.^[101] As mentioned previously, strain hardening is induced by the activation of different slip systems,^[102] and in order to accommodate for strain incompatibilities during plastic deformation, a minimum of five activated slip systems are required.^[103,104] The volume fraction of grains with at maximum three, four, five, six, seven or eight active

slip systems during four ECAP passes are predicted in Figure 16. In the first pass, approximately 80 pct of the grains deform with at least six active slip systems which could be attributed to the lower dislocation movement resistant that is exhibited by coarse grains. However, for the second pass, approximately 60 pct of the grains deform with at least six active slip systems. This volume fraction decreases with increasing number of passes, since it is estimated that 55 pct of the grains deform with at least six active slip systems for the third pass and 50 pct for the fourth pass. Furthermore, an increase in the volume fraction of grains deforming with a maximum of four active slip systems is observed with increasing number of passes. The correlation between slip activity and grain fragmentation reveals that grains fragmentation activity is proportional to the number of active slip system. Grain fragmentation is highly probable to occur in grains with at least 8 active slip systems. The volume fraction of grain fragmentation decreased with decreasing volume fraction of grains with at least eight active slip systems. Indeed, after the second pass, very little change is observed in the grains size with the texture reaching its ideal ECAP components.

4. Grain size

A microstructure with ultrafine grain size varying from a few microns to submicron can be obtained from severe plastic deformation processes such as ECAP. With a high level of plastic strain, the high internal energy stored in the grains is the result of the high dislocation densities that promote the formation of obstacles (GNDs) that hinder the motion of mobile dislocations. The increase in the internal energy of the grains leads to an increase in the misorientation angle between subgrains, and grain fragmentation occurs when this angle reaches a critical value (*i.e.*, the misorientation angle exceeds 5 deg). The new grains

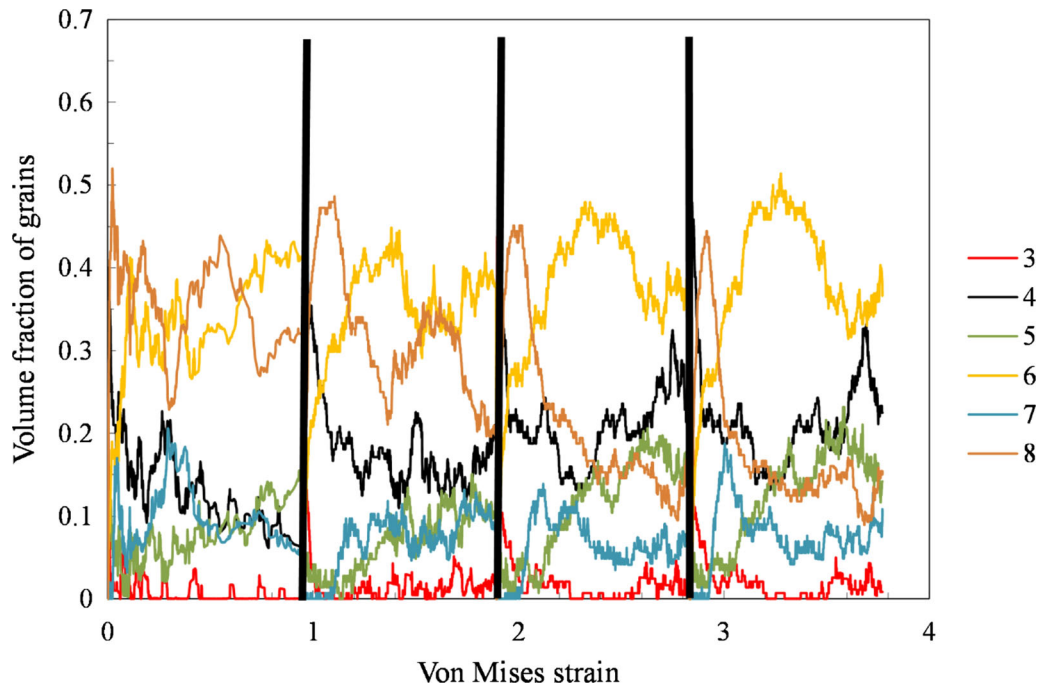


Fig. 16—Predicted volume fraction of grains with at maximum three, four, five, six, seven or eight active slip system during four ECAP passes.

are formed with a microstructure distinct from their parent grain in terms of dislocation density, grain size, and orientation.

In our grain fragmentation model, grains are subdivided initially into nine subgrains having similar microstructure and orientation to their parent grains, where each subgrain is assigned one-third of its parent grain size. As explained in Section III-B, each grain is allowed to exhibit three fragmentation levels, *i.e.*, $9 \times 9 \times 9 = 729$ new grains. Thus, a polycrystal with an average grain size of $80 \mu\text{m}$ can reach $80/27 = 2.96 \mu\text{m}$ as a minimum value after one pass of ECAP. After the 1A ECAP pass, the EBSD-measured average grain size of the aluminum alloy is found to be equal to $1.45 \mu\text{m}$, while the predicted value is equal to $3 \mu\text{m}$. An additional fragmentation level is necessary to capture the grain size after the first pass well; however, it is difficult to implement due to computational limitations. A better grain size prediction is achieved for the 2C ECAP pass. The experimental and the predicted average grain size in the 2C ECAP pass are equal to 1.11 and $1.02 \mu\text{m}$, respectively. Furthermore, a good prediction of the average grain size is obtained at the 4C ECAP pass, with an experimental value of $0.7 \mu\text{m}$ and a predicted value of $0.675 \mu\text{m}$.

C. Post-ECAP

As illustrated in Section IV-B-2, different microstructural features of the polycrystal are developed after severe plastic deformation. As the plastic strain increases, dislocations start to accumulate at the subgrain boundaries, forming low-angle grain boundaries. At higher levels of strain, the misorientation between subgrains increases and new grains are created with

relatively low dislocation density. Grain fragmentation occurs in order to release the stored energy in the polycrystal during deformation. As a consequence of grain fragmentation, the new fine grain boundaries hinder the dislocation movement by pinning them at the boundaries, thus reducing the mobile dislocation density. In order to predict the mechanical properties of the ECAPed samples, several simulations were performed. Figure 17 shows the true stress-true strain curves of the ECAPed aluminum alloy for one pass at room temperature. The model was used to predict the flow stress up to the UTS, since no damage formulation that can predict the flow stress response after necking is included in the current model. Although the predicted grain size after one pass is $3 \mu\text{m}$, simulations related to the measured grain size ($1.45 \mu\text{m}$) were performed for the sake of comparison with the experimental data. An excellent agreement can be seen between the predicted ($1.45 \mu\text{m}$) and the measured tensile behaviors. However, a shift of around 20MPa is revealed between the predicted ($3 \mu\text{m}$) and the measured tensile behaviors. This shift can be explained by the Hall-Petch relationship, where the flow stress is inversely proportional to the square root of the grain size, *i.e.*, larger grains lead to smaller stress. In addition, it can be seen from Figure 16 that the predictions in the extrusion direction are better than the predictions in the flow direction due to the texture developed during the ECAP process. The tensile behavior of the ECAPed aluminum alloy after 2C is plotted in Figure 18. For both strain rates, the model-generated curves are in accordance with the experimental curves for both the extrusion direction and the flow direction. Similarly, the predictions after the fourth pass of ECAP are in excellent agreement with

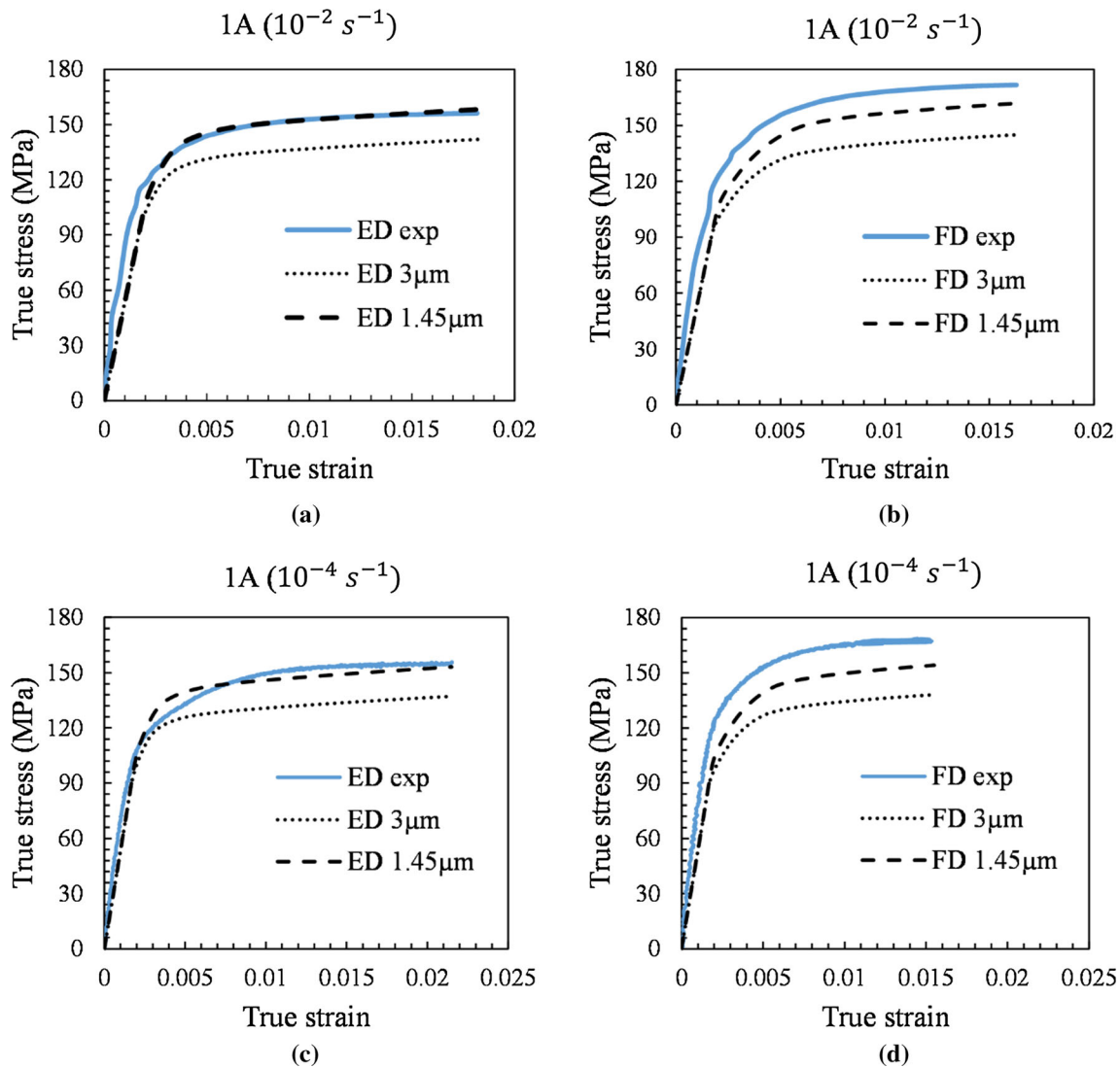


Fig. 17—Predictions of the stress-strain behavior of the ECAPed sample after one pass along ED: extrusion direction at strain rate (a) 10^{-2} s^{-1} (c) 10^{-4} s^{-1} and FD: flow direction at strain rate (b) 10^{-2} s^{-1} (d) 10^{-4} s^{-1} .

the experimental results for both strain rates and both directions, as shown in Figure 19.

V. CONCLUSIONS

In this work, the material mechanical, microstructural and textural behavior during equal channel angular pressing (ECAP) processes are modeled using a multi-scale framework that couples a crystal plasticity (CP) scheme with a continuum dislocation dynamics (CDD) model. The proposed multi-scale approach predicted the texture evolution, the statistically stored dislocations (SSDs) and the geometrically necessary dislocations (GNDs) densities evolutions, the microstructure evolution and finally the mechanical properties of the SPD processed material. The strain hardening in the model was considered to result from both the increase in the

dislocation density and the grain fragmentation. The grain fragmentation process was modeled by accounting for the grain-grain interaction and incorporating the concept of the geometrically necessary dislocations (GNDs) into the mean free path of the dislocations. GNDs result from grain boundaries restricting the free deformation of a grain, causing an internal plastic deformation gradient that subsequently leads to grain fragmentation. A commercial Al-1100 billet, with rolling texture, was ECAP processed at room temperature using route C. After a single pressing, a considerable refinement of the microstructure was observed (the grain size was reduced by 55 times), and the texture transformed into a shear-like texture rotated by an angle of 45 deg. The average grain size after one pass reduced from 80 to $1.45 \mu\text{m}$ and reached $0.7 \mu\text{m}$ after four passes. The yield strength of the as-received Al alloy increased drastically from 80 to 130 MPa after single pressing and to 160

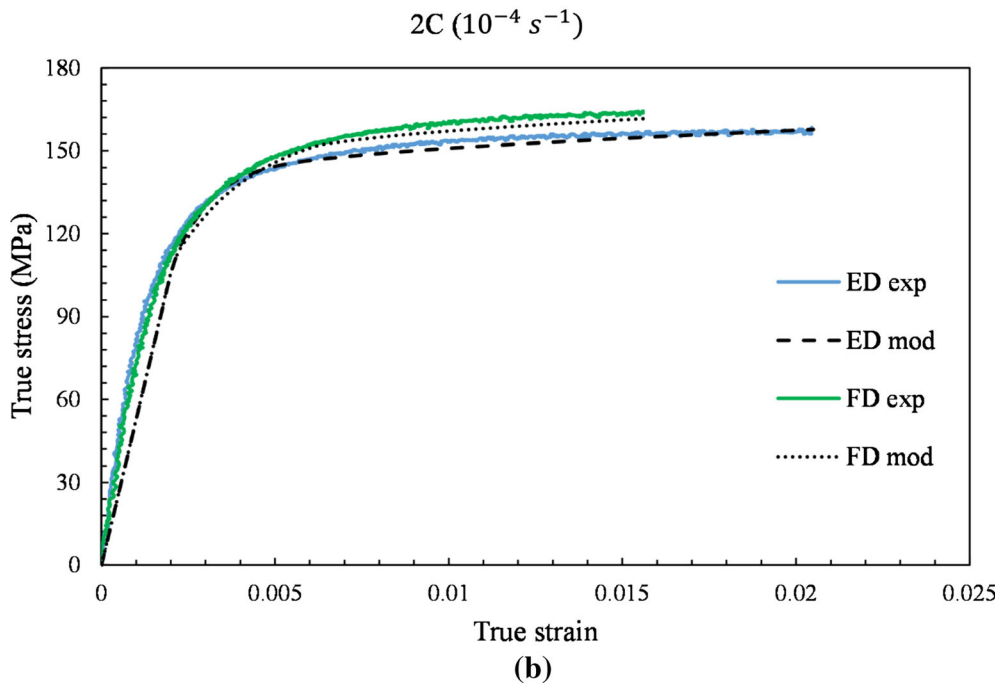
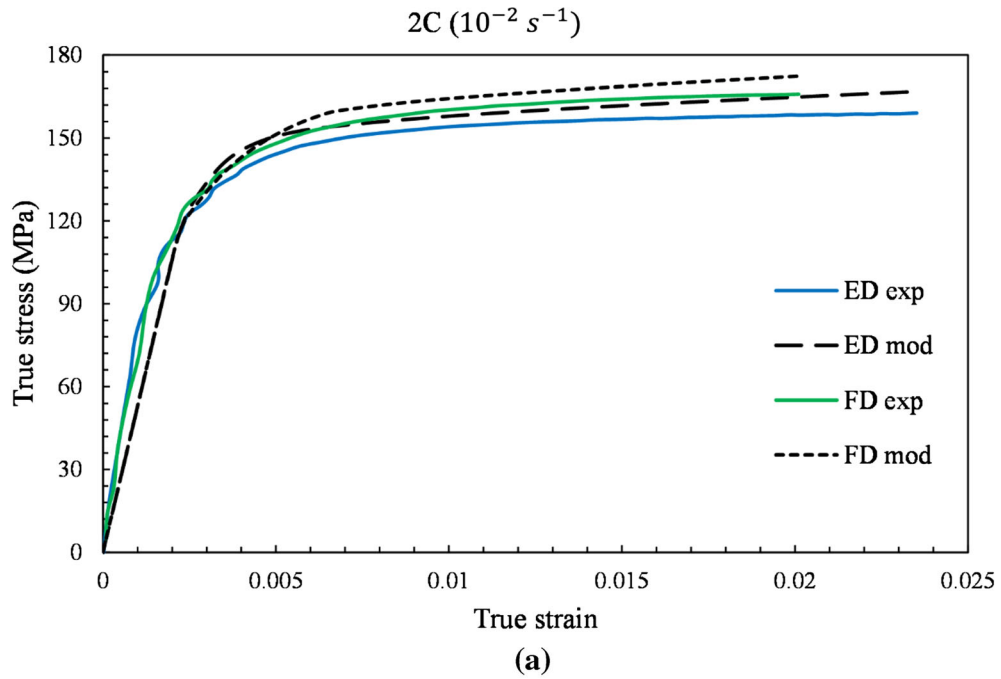


Fig. 18—Predictions of the stress-strain behavior of the ECAPed sample after the second pass at strain rate of (a) $10^{-2} s^{-1}$ (b) $10^{-4} s^{-1}$ (*ED* extrusion direction, *FD* flow direction).

MPa after four passes. The proposed model parameters were calibrated using the tensile true-stress true-strain curves of the unprocessed material at two strain rates. The ECAP-processed aluminum microstructure, texture

and dislocation densities were predicted. The model predicted an increase in the dislocation density during each ECAP pass, through generation and the multiplication of dislocations. Both mobile dislocations and

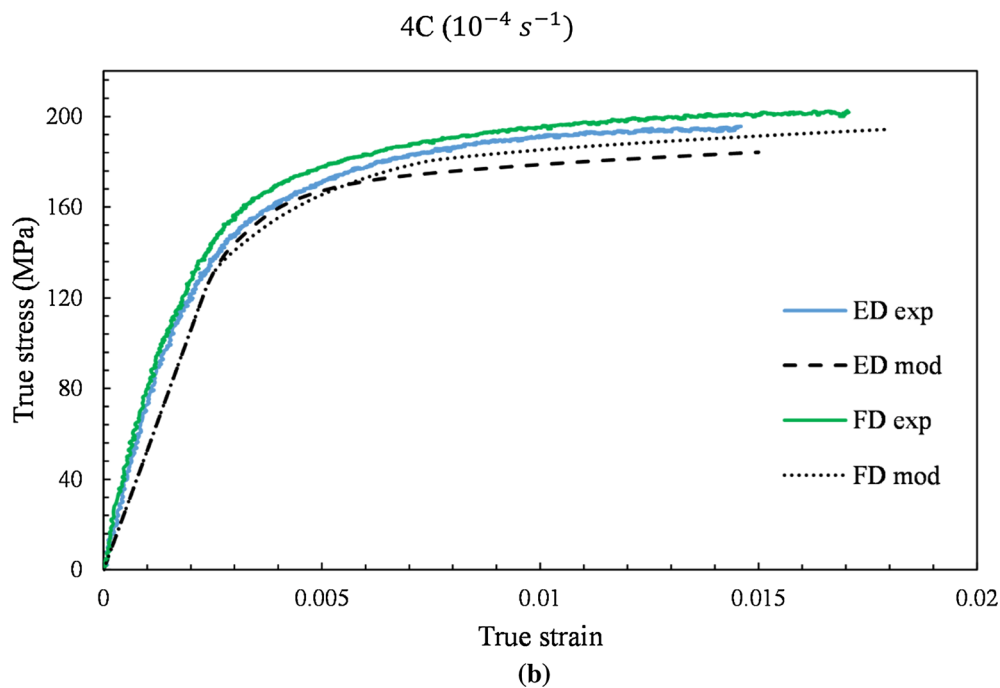
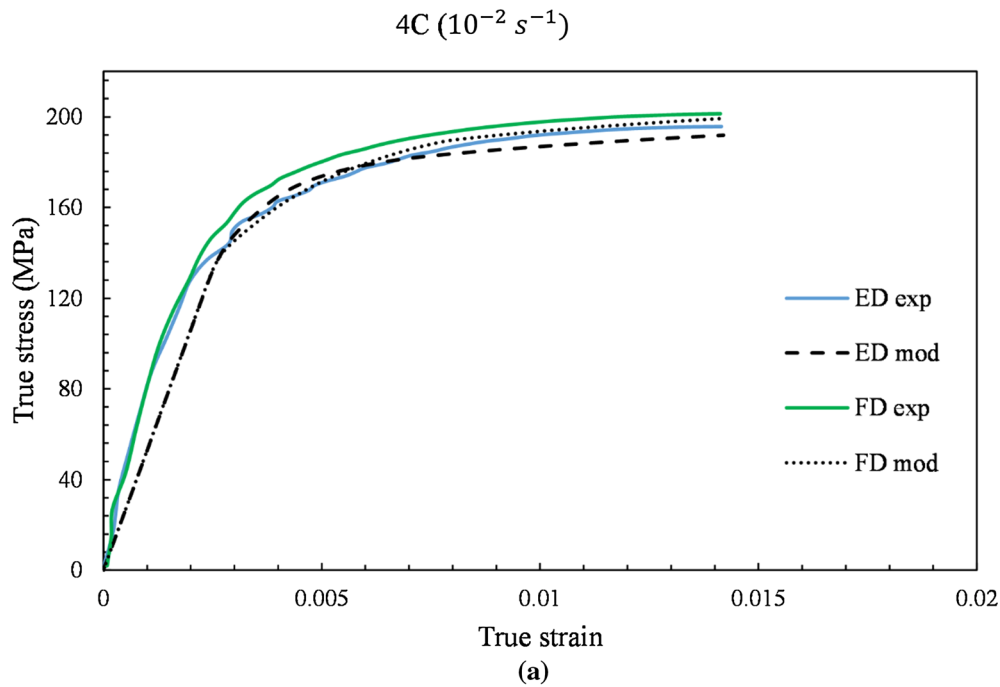


Fig. 19—Predictions of the stress-strain behavior of the ECAPed sample after the fourth pass at strain rate of (a) $10^{-2} s^{-1}$ (b) $10^{-4} s^{-1}$ (*ED* extrusion direction, *FD* flow direction).

GNDs increased similarly up to a threshold strain, beyond which the mobile dislocation evolution rate decreased. After three ECAP passes, the dislocation density increase rate slowed down significantly. The mechanical properties of the ECAP processed materials were predicted successfully by using the predicted texture, microstructure and dislocation densities.

ACKNOWLEDGMENTS

The authors would like to acknowledge the American University of Beirut (AUB) and the National Council for Scientific Research of Lebanon (CNRS-L) for granting a doctoral fellowship to Ali Al-Hadi Kobaissy.

DATA AVAILABILITY

The raw/processed data required to reproduce these findings cannot be shared at this time as the data also forms part of an ongoing study. The raw data required to reproduce these findings will be made available to download from [<https://deepblue.lib.umich.edu/data>].

REFERENCES

1. A. Azushima, R. Kopp, A. Korhonen, D.Y. Yang, F. Micari, G.D. Lahoti, P. Groche, J. Yanagimoto, N. Tsuji, A. Rosochowski, and A. Yanagida: *CIRP Ann.*, 2008, vol. 57, pp. 716–35.
2. V.M. Segal: Phys. Tech. Inst. Acad. Sci. Buelorussia, 1974.
3. V.M. Segal: *Mater. Sci. Eng. A.*, 1995, vol. 197, pp. 157–64.
4. V.M. Segal: *Mater. Sci. Eng. A*, 1999, vol. 271, pp. 322–33.
5. R.Z. Valiev and T.G. Langdon: *Prog. Mater. Sci.*, 2006, vol. 51, pp. 881–981.
6. I.J. Beyerlein and C.N. Tomé: *Int. J. Plast.*, 2007, vol. 23, pp. 640–64.
7. Z. Horita, T. Fujinami, and T.G. Langdon: *Mater. Sci. Eng. A.*, 2001, vol. 318, pp. 34–41.
8. L.S. Toth and C. Gu: *Mater. Charact.*, 2014, vol. 92, pp. 1–14.
9. A.S. Khan and C.S. Meredith: *Int. J. Plast.*, 2010, vol. 26, pp. 189–203.
10. I.J. Beyerlein and L.S. Tóth: *Prog. Mater. Sci.*, 2009, vol. 54, pp. 427–510.
11. K. Nakashima, Z. Horita, M. Nemoto, and T.G. Langdon: *Acta Mater.*, 1998, vol. 46, pp. 1589–99.
12. S. Li and O.V. Mishin: *Metall. Mater. Trans. A*, 2014, vol. 45A, pp. 1689–92.
13. S. Ferrasse, V.M. Segal, K.T. Hartwig, and R.E. Goforth: *Metall. Mater. Trans. A*, 1997, vol. 28A, pp. 1047–57.
14. M.H. Shaeri, M. Shaeri, M.T. Salehi, S.H. Seyyedain, and F. Djavanroodi: *Trans. Nonferr. Met. Soc. China*, 2015, vol. 25, pp. 1367–75.
15. V.V. Stolyarov and R. Lapovok: *J. Alloys Compd.*, 2004, vol. 378, pp. 233–36.
16. N.A. Krasil'nikov: *Russ. Metall.*, 2005, vol. 3, pp. 220–26.
17. M. Muzyk, Z. Pakielka, and K.J. Kurzydowski: *Scr. Mater.*, 2011, vol. 64, pp. 916–18.
18. N. Hansen and C.Y. Barlow: *Plastic Deformation of Metals and Alloys*, 5th ed., Elsevier, New York, 2014.
19. W.D. Kuhlmann: *Mater. Sci. Eng. A*, 1989, vol. 3, pp. 1–41.
20. B. Bay, N. Hansen, D.A. Hughes, and D. Kuhlmann-Wilsdorf: *Acta Metall. Mater.*, 1992, vol. 40, pp. 205–19.
21. D. Kuhlmann-Wilsdorf and N. Hansen: *Scripta Metall. Mater.*, 1991, vol. 25, pp. 1557–62.
22. A. Mishra, B.K. Kad, F. Gregori, and M.A. Meyers: *Acta Mater.*, 2007, vol. 55, pp. 13–28.
23. Y.L. Wei, A. Godfrey, W. Liu, Q. Liu, X. Huang, N. Hansen, and G. Winther: *Scripta Mater.*, 2011, vol. 65, pp. 355–58.
24. D. Kuhlmann-Wilsdorf: *Scripta Mater.*, 1997, vol. 36, pp. 173–81.
25. H.W. Zhang, X. Huang, and N. Hansen: *Acta Mater.*, 2008, vol. 56, pp. 5451–65.
26. N.Q. Chinh, T. Csanádi, J. Gubicza, and T.G. Langdon: *Acta Mater.*, 2010, vol. 58, pp. 5015–21.
27. N. Hansen, X. Huang, and D.A. Hughes: *Mater. Sci. Eng. A*, 2001, vol. 317, pp. 3–11.
28. D.A. Hughes and N. Hansen: *Acta Mater.*, 2000, vol. 48, pp. 2985–3004.
29. Y. Chen, Y. Li, L. He, C. Lu, H. Ding, and Q. Li: *Mater. Lett.*, 2008, vol. 62, pp. 2821–24.
30. M. Zehetbauer and V. Seumer: *Acta Metall. Mater.*, 1993, vol. 41, pp. 577–88.
31. M. Zehetbauer: *Acta Metall. Mater.*, 1993, vol. 41, pp. 589–99.
32. T. Sakai, A. Belyakov, R. Kaibyshev, H. Miura, and J.J. Jonas: *Prog. Mater. Sci.*, 2014, vol. 60, pp. 130–207.
33. N.Q. Chinh, G. Horváth, Z. Horita, and T.G. Langdon: *Acta Mater.*, 2004, vol. 52, pp. 3555–63.
34. D. Moldovan, D. Wolf, S.R. Phillpot, and A.J. Haslam: *Acta Mater.*, 2002, vol. 50, pp. 3397–3414.
35. D. Farkas, S. Mohanty, and J. Monk: *Mater. Sci. Eng. A*, 2008, vol. 493, pp. 33–40.
36. N. Hansen: *Scripta Mater.*, 2004, vol. 51, pp. 801–06.
37. Y.C. Chen, Y.Y. Huang, C.P. Chang, and P.W. Kao: *Acta Mater.*, 2003, vol. 51, pp. 2005–15.
38. W.H. Huang, C.Y. Yu, P.W. Kao, and C.P. Chang: *Mater. Sci. Eng. A.*, 2004, vol. 366, pp. 221–28.
39. I. Nikulin and R. Kaibyshev: *Mater. Sci. Forum*, 2012, vols. 715–716, pp. 317–22.
40. S.-Y. Chang, J.G. Lee, K.-T. Park, and D.H. Shin: *Mater. Trans.*, 2001, vol. 42, pp. 1074–80.
41. É.F. Prados, V.L. Sordi, and M. Ferrante: *Mater. Res.*, 2008, vol. 11, pp. 199–205.
42. J.H. Park, K.-T. Park, Y.S. Lee, and W.J. Nam: *Metall. Mater. Trans. A.*, 2005, vol. 36, pp. 1365–68.
43. Y.M. Wang and E. Ma: *Mater. Sci. Eng. A.*, 2004, vols. 375–377, pp. 46–52.
44. Y. Beygelzimer: *Mech. Mater.*, 2005, vol. 37, pp. 753–67.
45. A. Ostapovets, P. Šedá, A. Jäger, and P. Lejček: *Int. J. Plast.*, 2012, vol. 29, pp. 1–12.
46. L.S. Tóth, Y. Estrin, R. Lapovok, and C. Gu: *Acta Mater.*, 2010, vol. 58, pp. 1782–94.
47. M.J. Starink, X.G. Qiao, J. Zhang, and N. Gao: *Acta Mater.*, 2009, vol. 57, pp. 5796–5811.
48. H. Petryk and S. Stupkiewicz: *Mater. Sci. Eng. A.*, 2007, vol. 444, pp. 214–19.
49. R.A. Lebensohn and C.N. Tomé: *Acta Metall. Mater.*, 1993, vol. 41, pp. 2611–24.
50. N.A. Enikeev, M.F. Abdullin, A.A. Nazarov, and I.J. Beyerlein: *Int. J. Mater. Res.*, 2007, vol. 98, pp. 167–71.
51. A.A. Nazarov, N.A. Enikeev, A.E. Romanov, T.S. Orlova, I.V. Alexandrov, I.J. Beyerlein, and R.Z. Valiev: *Mater. Sci.*, 2006, vol. 54, pp. 985–95.
52. K. Frydrych and K. Kowalczyk-Gajewska: *Mater. Sci. Eng. A.*, 2016, vol. 658, pp. 490–502.
53. S.R. Kalidindi, B.R. Donohue, and S. Li: *Int. J. Plast.*, 2009, vol. 25, pp. 768–79.
54. K.H. Jung, D.K. Kim, Y.T. Im, and Y.S. Lee: *Int. J. Plast.*, 2013, vol. 42, pp. 120–40.
55. I.J. Beyerlein, R.A. Lebensohn, and C.N. Tomé: *Mater. Sci. Eng. A.*, 2003, vol. 345, pp. 122–38.
56. M. Seefeldt, L. Delannay, B. Peeters, S.R. Kalidindi, and P. Van Houtte: *Mater. Sci. Eng. A*, 2001, vol. 319, pp. 192–96.
57. A.E. Romanov and V.I. Vladimirov: *North Holland Amsterdam*, 1992, vol. 9, pp. 191–422.
58. A.H. Kobaissy, G. Ayoub, L.S. Toth, S. Mustapha, and M. Shehadeh: *Int. J. Plast.*, 2018, vol. 114, pp. 252–71.
59. A.S. Khan and J. Liu: *Int. J. Plast.*, 2016, vol. 86, pp. 56–69.
60. Y. Aoyagi, R. Kobayashi, Y. Kaji, and K. Shizawa: *Int. J. Plast.*, 2013, vol. 47, pp. 13–28.
61. N.C. Admal, G. Po, and J. Marian: *Int. J. Plast.*, 2018, vol. 106, pp. 1–30.
62. C.F.O. Dahlberg, J. Faleskog, C.F. Niordson, and B.N. Legarh: *Int. J. Plast.*, 2013, vol. 43, pp. 177–95.
63. S. Wulfinghoff, E. Bayerschen, and T. Böhlke: *Int. J. Plast.*, 2013, vol. 51, pp. 33–46.
64. M.E. Gurtin: *Int. J. Plast.*, 2008, vol. 26, pp. 1073–96.
65. O. Daaland and E. Nes: *Acta Mater.*, 1996, vol. 44, pp. 1389–411.
66. M. Zecevic, R.A. Lebensohn, R.J. McCabe, and M. Knezevic: *Int. J. Plast.*, 2018, vol. 109, pp. 193–211.
67. A.A. Ridha and W.B. Hutchinson: *Acta Metall.*, 1982, vol. 30, pp. 1929–39.
68. S. Huang and A.S. Khan: *Int. J. Plast.*, 1992, vol. 8, pp. 501–17.
69. J. Hirsch and T. Al-Samman: *Acta Mater.*, 2013, vol. 61, pp. 818–43.
70. B. Poorganji, P. Sepehrband, H. Jin, and S. Esmaili: *Scripta Mater.*, 2010, vol. 63, pp. 1157–60.
71. E.A. El-Danaf, M.S. Soliman, A.A. Almajid, and M.M. El-Rayes: *Mater. Sci. Eng. A.*, 2007, vol. 458, pp. 226–34.
72. J.K. Kim, H.K. Kim, J.W. Park, and W.J. Kim: *Scripta Mater.*, 2005, vol. 53, pp. 1207–11.

73. G.I. Taylor: *J. Inst. Met.*, 1938, vol. 62, pp. 307–25.
74. T.H. Lin: *J. Mech. Phys. Solids.*, 1957, vol. 5, pp. 143–49.
75. N. Zouhal, A. Molinari, and T.S. Toth: *Int. J. Plast.*, 1996, vol. 12, pp. 343–60.
76. E.H. Lee: *J. Appl. Mech.*, 1969, vol. 36, pp. 1–6.
77. E. Orowan: *Proc. Phys. Soc.*, 1940, vol. 52, p. 8.
78. D. Li, H. Zbib, X. Sun, and M. Khaleel: *Int. J. Plast.*, 2014, vol. 52, pp. 3–17.
79. H. Lyu, A. Ruimi, and H.M. Zbib: *Int. J. Plast.*, 2015, vol. 72, pp. 44–59.
80. H. Gao and Y. Huang: *Scr. Mater.*, 2003, vol. 48, pp. 113–18.
81. T. Ohashi, M. Kawamukai, and H. Zbib: *Int. J. Plast.*, 2007, vol. 23, pp. 897–914.
82. T. Ohashi: *Int. J. Plast.*, 2005, vol. 21, pp. 2071–88.
83. F. Nye: *Acta Metall.*, 1953, vol. 1.
84. P.J. Konijnenberg, S. Zaeferrer, and D. Raabe: *Acta Mater.*, 2015, vol. 99, pp. 402–14.
85. L.S. Tóth, R.A. Massion, L. Germain, S.C. Baik, and S. Suwas: *Acta Mater.*, 2004, vol. 52, pp. 1885–98.
86. S. Li, I.J. Beyerlein, and M.A.M. Bourke: *Mater. Sci. Eng. A.*, 2005, vol. 394, pp. 66–77.
87. S. Li: *Trans. Nonferrous Met. Soc. China.*, 2013, vol. 23, pp. 170–79.
88. C.F. Gu, L.S. Tóth, and C.H.J. Davies: *Scripta Mater.*, 2011, vol. 65, pp. 167–70.
89. Y. Estrin and H. Mecking: *Acta Metall.*, 1984, vol. 32, pp. 57–70.
90. H. Mecking and U.F. Kocks: *Acta Metall.*, 1981, vol. 29, pp. 1865–75.
91. Y. Estrin, L.S. Tóth, A. Molinari, and Y. Bréchet: *Acta Mater.*, 1998, vol. 46, pp. 5509–22.
92. L.S. Toth, P. Gilormini, and J.J. Jonas: *Acta Metall.*, 1988, vol. 36, pp. 3077–91.
93. H. Hallberg, M. Wallin, and M. Ristinmaa: *Mater. Sci. Eng. A.*, 2010, vol. 527, pp. 1126–34.
94. M.H. Shaeri, M. Shaeri, M. Ebrahimi, M.T. Salehi, and S.H. Seyyedein: *Prog. Nat. Sci. Mater. Int.*, 2016, vol. 26, pp. 182–91.
95. C.V. Venkatesh, S.G.S. Raman, and U. Chakkingal: *Trans. Indian Inst. Met.*, 2013, vol. 66, pp. 147–54.
96. M. Howeyze, H. Arabi, A.R. Eivani, and H.R. Jafarian: *Mater. Sci. Eng. A*, 2018, vol. 720, pp. 160–68.
97. M. Howeyze, A.R. Eivani, H. Arabi, and H.R. Jafarian: *Mater. Sci. Eng. A*, 2018, vol. 732, pp. 120–28.
98. S.E. Mousavi, M.H. Khaleghifar, M. Meratian, B. Sadeghi, and P. Cavaliere: *Materialia*, 2018, vol. 4, pp. 310–22.
99. M. Miraglia, P. Dawson, and T. Leffers: *Acta Mater.*, 2007, vol. 55, pp. 799–812.
100. T. Hama and H. Takuda: *Int. J. Plast.*, 2011, vol. 27, pp. 1072–92.
101. G. Winther: *Acta Mater.*, 2003, vol. 51, pp. 417–29.
102. G. Gottstein: *Physikalische Grundlagen Der Materialkunde*, Springer, Berlin, 1998.
103. G.I. Taylor: *J. Inst. Met.*, 1938, vol. 62, pp. 307–24.
104. R. Von Mises: *Zeitschrift Fur Angew. Math. Und Mech.*, 1928, vol. 8, pp. 161–85.

Publisher's Note Springer Nature remains neutral with regard to jurisdictional claims in published maps and institutional affiliations.